DOI: 10.1111/phor.12460

ORIGINAL ARTICLE

# A point cloud filtering method based on anisotropic error model

Mustafa Ozendi[1] | Devrim Akca[2] | Hüseyin Topan[1]

[1]Department of Geomatics Engineering, Zonguldak Bülent Ecevit University, Zonguldak, Turkey

[2]Department of Civil Engineering, Isik University, Istanbul, Turkey

**Correspondence**
Hüseyin Topan and Mustafa Ozendi, Department of Geomatics Engineering, Zonguldak Bülent Ecevit University, Zonguldak, Turkey.
Email: topan@beun.edu.tr and mozendi@gmail.com

**Funding information**
infoTRON; Türkiye Bilimsel ve Teknolojik Araştırma Kurumu; Zonguldak Bülent Ecevit Üniversitesi

## Abstract

Many modelling applications require 3D meshes that should be generated from filtered/cleaned point clouds. This paper proposes a methodology for filtering of terrestrial laser scanner (TLS)-derived point clouds, consisting of two main parts: an anisotropic point error model and the subsequent decimation steps for elimination of low-quality points. The point error model can compute the positional quality of any point in the form of error ellipsoids. It is formulated as a function of the angular/mechanical stability, sensor-to-object distance, laser beam's incidence angle and surface reflectivity, which are the most dominant error sources. In a block of several co-registered point clouds, some parts of the target object are sampled by multiple scans with different positional quality patterns. This situation results in redundant data. The proposed decimation steps removes this redundancy by selecting only the points with the highest positional quality. Finally, the Good, Bad, and the Better algorithm, based on the ray-tracing concept, was developed to remove the remaining redundancy due to the Moiré effects. The resulting point cloud consists of only the points with the highest positional quality while reducing the number of points by factor 10. This novel approach resulted in final surface meshes that are accurate, contain predefined level of random errors and require almost no manual intervention.

**KEYWORDS**
error ellipsoid, point clouds, point error model, quality evaluation, surface reconstruction, terrestrial laser scanning

## INTRODUCTION

Over the past decade, the need for high-quality geospatial data has driven the development of terrestrial laser scanner (TLS) technology; these advances have also allowed TLS applications to expand into a wide variety of fields, including construction, cultural heritage, surveying and forestry. One application of TLS-captured point cloud data is three-dimensional (3D) surface mesh generation of objects (e.g., statues, monuments and buildings), which has also found wide application in archaeology, architecture and civil engineering (Akca et al., 2006, 2007; Pu, 2008; Xingchang & Xianlin, 2006). From a user's perspective, the ability to quantify and exclude erroneous points, the overall accuracy of the surface mesh model generated, the resolution of the object's details and how these factors come to affect in real-world applications, are of primary concern.

TLSs capture the geometry of the target object in the form of a dense point cloud, usually consisting of millions of data points. Each data point is subject to random errors, which propagate through the surface mesh reconstruction steps and thus significantly impact the accuracy of the final product. Consequently, the ability to estimate the random error pattern of each point is critical to assessing the overall quality of the point cloud data and the final product (3D model). Random errors are the small (accidental) differences between the different measurements of the same thing. They obey the laws of probability and are sometimes called noise or accidental errors.

TLS measurement precision is affected by the distance from the scanner to the object, the incidence angle of the signal, the reflectance property of the object and the mechanical stability of the (vertical and horizontal) angular encoders of the device. Thus far, research has focused on the derivation of standard deviations of distance measurements to model point errors (Ge & Wunderlich, 2016; Wujanz et al., 2018). TLS manufacturer-provided precisions can also be used for error modelling, but they neglect anisotropic error sources. Generally, these error modelling methods fall short because they consider error parameters individually; the full range of error components are not factored into a total error budget of the data points. There is a clear need for a comprehensive solution that considers all error components, but also a solution that is practical, time and work efficient, and independent of TLS factory specifications.

Additionally, to ensure complete coverage for surface mesh generation, the target object needs to be scanned from multiple locations; this configuration often results in overlapping scans of the target object, where some parts are redundantly captured in multiple point clouds. Each of these point clouds has a different error pattern, so any 3D surface mesh generated from them will contain varying quality zones, interfering with each other, and appearing as significant noise and defects on the final model. Moreover, these duplications also cause excessive processing times for the 3D surface triangulation. In current practice, the solution to this problem is resampling the point cloud, which decreases the number of points by averaging the original positions of points. Some studies modify the point cloud by shifting the positions of the points using advanced statistical methods (Jones et al., 2003; Liu et al., 2012). However, these solutions are not optimal because they neglect both the anisotropic error pattern of the individual points and how these errors propagate through surface mesh generation.

This study has two primary objectives:

- The first is to develop a generic and anisotropic point error model. The positional quality (spatial quality of the *X*, *Y* and *Z* coordinates) of any point acquired by TLS depends on object- and sensor–space error sources; this results in an anisotropic error pattern for scan data points. The point error model proposed in this study can compute a priori random error pattern of each point in the form of error ellipsoids. Error ellipsoid is a graphical representation for the theoretical precisions of the *X*, *Y* and *Z* coordinates a point.

- The second is to develop a point cloud decimation method that exploits the quality metrics estimated by this point error model. Following co-registration, the target object is sampled redundantly through multiple scans. Some parts of the target object are sampled using a mixture of points with high and low positional quality. The proposed method can solve this redundancy problem by using the low-quality point elimination methods, which take full advantage of the developed point error model.

The remainder of the paper is structured as follows. The Related Works section provides an overview of works related to point error models for TLS-derived point clouds and the error consideration in surface mesh generation. The Anisotropic Point Error Model section presents the proposed anisotropic point error model, considering the most significant sensor- and object–space error sources. The Least Errors Surface Reconstruction section presents the point cloud decimation method, which concludes in a least error surface reconstruction solution. The Experiments and Results section presents the experimental results. Finally is the Conclusions section.

## RELATED WORKS

### Point error model

TLSs measure the range (distance between the TLS and the target object), the horizontal and vertical angles, and the intensity of the reflected signal. The positional uncertainty of any measured point depends on these direct observations' a priori precisions.

Range measurement precision is affected by three major object space parameters: The distance between the TLS and the target object, the object's surface reflectivity, and the incidence angle of the signal. In an early work, Hebert and Krotkov (1992) experimentally investigated the effects of incidence angle and target distance; they found a significant discrepancy between the theoretical sensor characteristics and the observed performance. Several later studies modelled the range error algebraically only using the covariance matrices without considering these physical parameters (Guehring, 2001; Okatani & Deguchi, 2002; Sagawa et al., 2002; Williams et al., 1999). This approach was further improved by investigating the effect of surface reflectance on the ranging error (Sagawa et al., 2005, 2006). Angular errors and scanning geometry were also investigated, and the related calibration parameters were estimated in Lichti (2007, 2010).

TLS manufacturers also provide precisions, or so-called uncertainty values, that can be used in point error modelling. These values are provided in various formats. For instance, Bae et al. (2009) present the positional uncertainty of points as a closed-form expression, which considers the ranging uncertainty depending on the incidence angle and the angular uncertainty provided by the manufacturer. Similarly, Scaioni (2012) and Barbarella et al. (2017) present a stochastic model developed by computing the covariance matrix of each point by using the manufacturer-provided values. Mezian et al. (2016) also performed similar work for the mobile laser scanning (MLS) datasets. However, the studies using the manufacturer-provided precisions either lack anisotropic errors or ignore some (or all) of the object–space error sources, hence they may not be practical in implementation. The work presented by Stenz et al. (2020) differs from the others by developing a function for the range measurement precision, but only regarding the intensities.

The incidence angle, the angle between the incoming laser beam and the surface normal, plays a vital role in the range precision. Numerous studies have attempted to determine the relationship between the incidence angle and the range precision. In general, this relationship is quantified as the cosine of the incidence angle (Chen et al., 2017; Hebert & Krotkov, 1992; Soudarissanane et al., 2011; Young Min et al., 2008). Together with the manufacturer-provided angular precisions, this formulation was used to estimate the covariance matrix of a point in Grant et al. (2012a). Chen et al. (2015, 2016) and Ge and Wunderlich (2016) divided the manufacturer-provided

range precision by the cosine of the incidence angle to obtain the corrected range precision. Chen et al. (2015, 2016) used this corrected range precision, with the manufacturer-provided angular precisions, to compute the error ellipsoid of each point. In Hartzell et al. (2015), the error budget of points is quantised as a function of incidence angle, range and terrain morphology. However, their model omits the remaining object–space parameters such as the reflectance. Manufacturer provided precisions can also be used for computation of point uncertainty values ignoring some object space parameters as shown in Winiwarter et al. (2021).

The reflectance property of the target object also has a significant effect on the range precision. It is measured as an intensity value by the advanced TLS brands, while this capability has progressed in the last decade. In an early study, Hodge (2010) weighted the TLS's points according to the laser intensity and cosine of the incidence angle in a simulation study. A very comprehensive work, accounting for all error sources both in the object–space (distance between the scanner and the object, incidence angle of the signal and the intensity value of the returning signal) and in the sensor–space (mechanical stability of the vertical and horizontal angle measurement units), was given by Ozendi et al. (2016, 2017). They performed data- and model-driven experiments to show the suitability of a quadratic function. Another experimental study investigated the relationship between ranging uncertainty and both incidence angle and target object colour presented in Bolkas and Martinez (2018). Wujanz et al. (2017, 2018) and Kermarrec et al. (2018) formulated the range precision as a power function of the raw intensities captured by the TLS device. This method is applicable only for those TLS brands, which allow access to the raw intensities. Recently, the relationship between the range precision and the surface reflectivity was modelled by a polynomial function by Schmitz et al. (2019) and Tan et al. (2018).

The primary deficiencies with the above methods are as follows:

- The majority of these studies focus on either range precision or angular precision individually, when the total error budget of a point depends on both range precision and angular precisions.
- Further, the most critical parameters affecting the range precision are the distance between TLS and target object, the incidence angle, and the surface reflectance properties. So far, however, the majority of studies have not developed a model that takes all these parameters into account.
- The optimal point error model should not be sensor dependent or not solely rely on the manufacturer-provided information. A practical approach, together with on-the-job instructions, is required to estimate the a priori precisions of the direct TLS observations.
- Each point's uncertainty should be calculated individually since the point cloud data has an anisotropic error pattern.

## Error consideration in mesh reconstruction

A point cloud acquired by a scanner inevitably contains errors, which depend on the sensor–space and the object–space parameters. Consequently, surface meshes generated from such points whose errors are above a specific limit are often of poor quality. Researchers have developed methods that generally utilise the neighbourhood information either at the point cloud or surface mesh level to deal with errors.

### Methods applied on the point cloud level

Pauly (2003) computes an error quadric for each point using tangent planes; these computed error quadrics are then employed to eliminate errors and simplify the point cloud. Weyrich et al. (2004) developed a toolbox to eliminate erroneous points with user interaction before surface mesh reconstruction.

Detection and removal of erroneous points can be performed by analysing the neighbourhood of points. For example, the mean-shift-based algorithm (Liu et al., 2012) iteratively shifts the point positions based on the

average position of its neighbours. The standard deviation of neighbouring points can also be used (Wang, Xu, et al., 2013). Another neighbourhood-based method establishes the neighbourhood relationships and checks if points satisfy this relationship. The points not satisfying this relationship are marked as outliers and removed (Wang, Liu, & Qin, 2013). The neighbourhood of any point can also be investigated by weighting each point using covariance analysis (Ohtake et al., 2005). Similarly, Schall et al. (2005) use covariance matrix analysis to eliminate erroneous points. Here, covariance matrix computation is performed using the plane fitting parameters. In a similar study, Marton et al. (2009) compute the weighted least squares plane for each point and then use the normal vector of this plane as the local surface normal.

In addition to plane fitting, sphere fitting can also be used (Guennebaud & Gross, 2007). Another covariance matrix-based method is presented by Adamson and Alexa (2006), which defines the weight function for each point. These weight functions are used to compute the covariance matrix of each point, and finally, an ellipsoid is computed from these covariance matrices. These ellipsoids are used to generate the point set surfaces rather than the triangular surface meshes. Baselgia et al. (2014) differ from the others in that they factor in both the scanning geometry and the surface's reflectivity in the weight calculation of each point.

### Methods applied at the surface mesh level

Noise at the mesh level can be removed non-iteratively by defining a local first-order predictor based on robust statistics (Jones et al., 2003). This method not only reduces the noise but also preserves details. Curvature is an important quantity in 3D modelling because it can be used to de-noise the surface mesh anisotropically. The method proposed by Hildebrandt and Polthier (2004) defines an anisotropic mean curvature-based shape operator for smoothing the mesh. Not only noise but also outlier can also be investigated in point clouds by means of curvature as shown in Sofia et al. (2013). There are several surface mesh generation algorithms. Among these, Delaunay 2.5D XY plane, Delaunay 2.5D Best Fitting Plane and Mesh from Points were investigated in terms of accuracy using a reference dataset by Long et al. (2018). Parametric surface models such as T-splines can be used for approximating TLS-generated point clouds and for accuracy assessment (Kermarrec et al., 2021).

The primary deficiencies of the above methods are as follows:

- Though many methods have been proposed for surface mesh reconstruction from point clouds, they commonly ignore error sources. None factor in both the sensor- and object–space error source parameters together. The most significant parameters are angular (mechanical) stability, sensor-to-object distance, incidence angle of the incoming laser beam and surface reflectivity. Most studies modify the point cloud by shifting the position of the points using advanced statistical methods.
- Moreover, for those approaches implementing novel surface mesh generation methods, the question remains unanswered as to how these methods can be applied to the point clouds obtained with TLSs.

## Contributions

This paper presents a novel point cloud decimation methodology suitable for use in surface mesh reconstruction tasks. It is in two main parts:

- A generic and anisotropic point error model was developed that can compute the positional uncertainty of each point in the form of error ellipsoids. Positional uncertainty is formulated explicitly as a function of the most dominant sensor- and object-space error sources, for example, angular (mechanical) stability, sensor-to-object distance, incidence angle of the incoming laser beam and surface reflectivity, so that each point's error

distribution pattern is treated in an anisotropic or heteroscedastic (point dependent) way. This model can be applied to all TLS brands with minimal fieldwork and implementation effort.

- A stochastic surface mesh-generation method keeps high positional quality points for meshing and removes those with low positional quality. The positional quality of any point is quantified using the error ellipsoid parameters. The consecutive decimation methods for eliminating the points with low positional quality are proposed. In contrast to the previous studies mentioned above, the proposed method does not necessarily need pre- or post-processes, such as outlier filtering or mesh smoothing, because the low-quality points that cause artefacts in the final surface mesh have already been removed.

## ANISOTROPIC POINT ERROR MODEL

The TLS mechanism operates in a spherical coordinate system and measures the range ($\rho$), vertical ($\alpha$) and horizontal ($\theta$) angles as direct observations (Figure 1).

Any point in this spherical coordinate system is defined as $\boldsymbol{r}_i = \left[\rho_i \;\; \alpha_i \;\; \theta_i\right]^T$, where $i$ is the index of the point in the point cloud. The Cartesian coordinates $\left[\begin{array}{ccc} x_i & y_i & z_i \end{array}\right]$ of the $i$-th point can be calculated straightforwardly using these direct observations:

$$\left[\begin{array}{c} x_i \\ y_i \\ z_i \end{array}\right] = \left[\begin{array}{c} \rho_i \cos(\alpha_i)\cos(\theta_i) \\ \rho_i \cos(\alpha_i)\sin(\theta_i) \\ \rho_i \sin(\alpha_i) \end{array}\right]. \tag{1}$$

Even though all TLSs provide the Cartesian coordinate values to the user, many do not provide the spherical coordinate values. In this case, the reverse transformation from the Cartesian coordinates can be performed using the following equations:

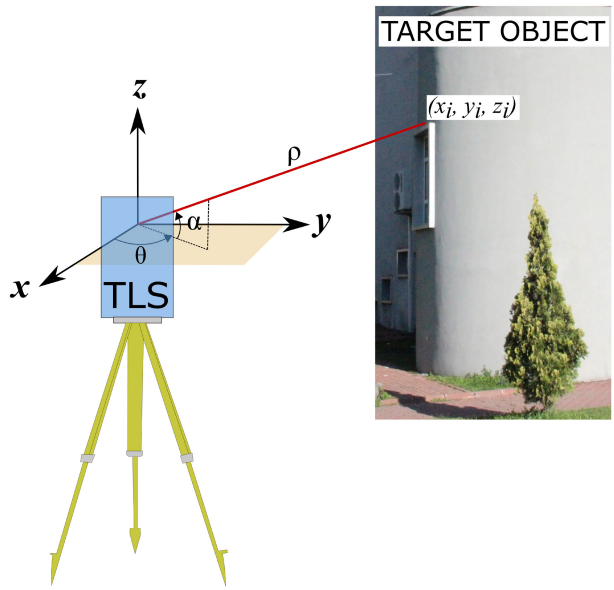


**FIGURE 1** Direct observations of a terrestrial laser scanner (TLS).

$$\boldsymbol{r}_i = \begin{cases} \rho_i = \sqrt{x_i^2 + y_i^2 + z_i^2} \\ \alpha_i = \tan^{-1}\left(\dfrac{z_i^2}{\sqrt{x_i^2 + y_i^2}}\right) \\ \theta_i = \tan^{-1}\left(\dfrac{y_i^2}{x_i^2}\right) \end{cases}. \tag{2}$$

The covariance matrix of any point $\boldsymbol{r}_i$ in the spherical coordinate system can be established using a priori precisions of the direct observations $(\rho_i, \alpha_i, \theta_i)$ given in Equation (3):

$$\sum_{\boldsymbol{rr}} = \begin{bmatrix} \sigma_\rho^2 & 0 & 0 \\ 0 & \sigma_\alpha^2 & 0 \\ 0 & 0 & \sigma_\theta^2 \end{bmatrix} \tag{3}$$

where $\sigma_\rho^2$, $\sigma_\alpha^2$ and $\sigma_\theta^2$ represent a priori variances of the range ($\rho$), vertical ($\alpha$) and horizontal ($\theta$) angle measurements, respectively. The off-diagonal elements are the covariances between the different pairs of the measurements. They are set to zero provided that the following two assumptions are held:

- The TLS is correctly calibrated at the factory, so there is no systematic error in the observations; this prevents any possible algebraic correlation between the observations.
- There is no physical correlation between the observations. This assumption is valid since the range and angle measurement units are independent of each other. The range measurement is performed using either time-of-flight or phase measurement technique through the optical telescope system. The angle measurements are performed electro-optically using high-resolution vertical and horizontal angular encoders, which are physically separated (Ingensand, 2006; Schulz, 2008).

The covariance matrix of any point in the Cartesian coordinate system, denoted as $\sum_{\mathbf{xx}}$ can be calculated using the law of error propagation.

$$\sum_{\mathbf{xx}} = \mathbf{J}_{\mathbf{xr}} \sum_{\mathbf{rr}} \mathbf{J}_{\mathbf{xr}}^{\mathbf{T}} \tag{4}$$

where $\mathbf{J}_{\mathbf{xr}}$ is the Jacobian matrix, which is established by partial derivatives of the Cartesian coordinates (Equation 1) with respect to the direct observations range ($\rho$), vertical ($\alpha$) and horizontal ($\theta$) angle, as shown in the following equation:

$$\mathbf{J}_{\mathbf{xr}} = \begin{bmatrix} \dfrac{\partial x_i}{\partial \rho} & \dfrac{\partial x_i}{\partial \alpha} & \dfrac{\partial x_i}{\partial \theta} \\ \dfrac{\partial y_i}{\partial \rho} & \dfrac{\partial y_i}{\partial \alpha} & \dfrac{\partial y_i}{\partial \theta} \\ \dfrac{\partial z_i}{\partial \rho} & \dfrac{\partial z_i}{\partial \alpha} & \dfrac{\partial z_i}{\partial \theta} \end{bmatrix}. \tag{5}$$

The parameters of the error ellipsoid can be calculated from the principal components of the covariance matrix $\sum_{\mathbf{xx}}$. This is achieved by solving the eigenvalue problem given in Equation (6):

$$\left(\sum_{\mathbf{xx}} - \lambda \mathbf{I}\right)\mathbf{z} = \mathbf{0} \tag{6}$$

where **I** is the unit matrix, elements of $\lambda = \begin{bmatrix}\lambda_1 & \lambda_2 & \lambda_3\end{bmatrix}$ are the eigenvalues and $\boldsymbol{z} = [z_1\ z_2\ z_3]$ is the eigenvector of $\sum_{xx}$.

An error ellipsoid is parameterised in its semi-axis dimensions and orientation, which correspond to the above eigenvalues and eigenvector, respectively.

The semi-axes dimensions are the square roots of the eigenvalues $(\sqrt{\lambda_1}, \sqrt{\lambda_2}, \sqrt{\lambda_3})$. Orientation of the ellipsoid is calculated using the eigenvector $\boldsymbol{z} = [z_1\ z_2\ z_3]$:

$$\text{Vertical Direction} = \tan^{-1}\left(\frac{z_3}{\sqrt{z_1^2 + z_2^2}}\right) \tag{7}$$

$$\text{Horizontal Direction} = \tan^{-1}\left(\frac{z_1}{z_2}\right). \tag{8}$$

The major axis of the error ellipsoid is aligned with the laser beam vector. This situation indicates that line of sight direction error is higher than those in the lateral directions.

Error ellipsoids are valuable metrics to investigate the magnitude and direction of the uncertainty pattern of the TLS-derived point observations. In order to derive the error ellipsoid of every individual point, a priori precisions of the angular $(\sigma_\alpha, \sigma_\theta)$ and range $\sigma_\rho$ measurements should be computed and inputted into the covariance matrix $\sum_{rr}$ in Equation (3). The practical methods are presented in the following two subsections to compute the angular and range measurements' a priori precisions.

## Derivation of the angular precision values ($\sigma_\alpha$ and $\sigma_\theta$)

Unlike the range measurement, angular measurements in TLSs are independent of the object–space conditions such as surface reflectivity, ambient temperature, humidity and distance. Angular precision measures how close the repeated angular measurements are performed; it is the result of the mechanical stability of the movement of the laser beamer in the vertical and horizontal directions. The higher the precision, the less scattering of the vertical and horizontal angles resulting from the repetitive scans. Vertical and horizontal angle precisions are the sensor–space parameters. Therefore, one set of vertical and horizontal angle precisions is constant in all scan files of a scanning campaign; they are project invariant values.

A practical measurement configuration for deriving the angular precisions is proposed. The outline is shown as a workflow diagram in Figure 2. It is based on static and repetitive measurements. In this configuration, the same scene is scanned repetitively, while the TLS remains stationary. Therefore, it is expected that each point should coincide with its conjugates in the other scans. However, the imperfect mechanical structure of the angular encoders causes deviations in the conjugate point positions of the same laser ray. These deviations along the vertical and horizontal directions are closely related to the vertical and horizontal angle precision of the TLS. Relevant studies are given in Parian and Gruen (2005), Schulz (2008) and Chow et al. (2010).

The same scene was scanned five times from the same scan station. First, four rays, each of which was in one of the four cardinal directions, were selected. Then, the conjugate points corresponding to these rays from five scans were selected according to their column/row numbers in the scan files. Four rays from five scan files correspond to $4 \times 5 = 20$ points in total. Next, using Equation (2), vertical ($\alpha$) and horizontal ($\theta$) angles of the conjugate points were computed. Then, for each direction, the root mean square errors (RMSEs) for both vertical ($\alpha$) and horizontal ($\theta$) angles were computed. Finally, a priori angular precisions $(\sigma_\alpha, \sigma_\theta)$ were

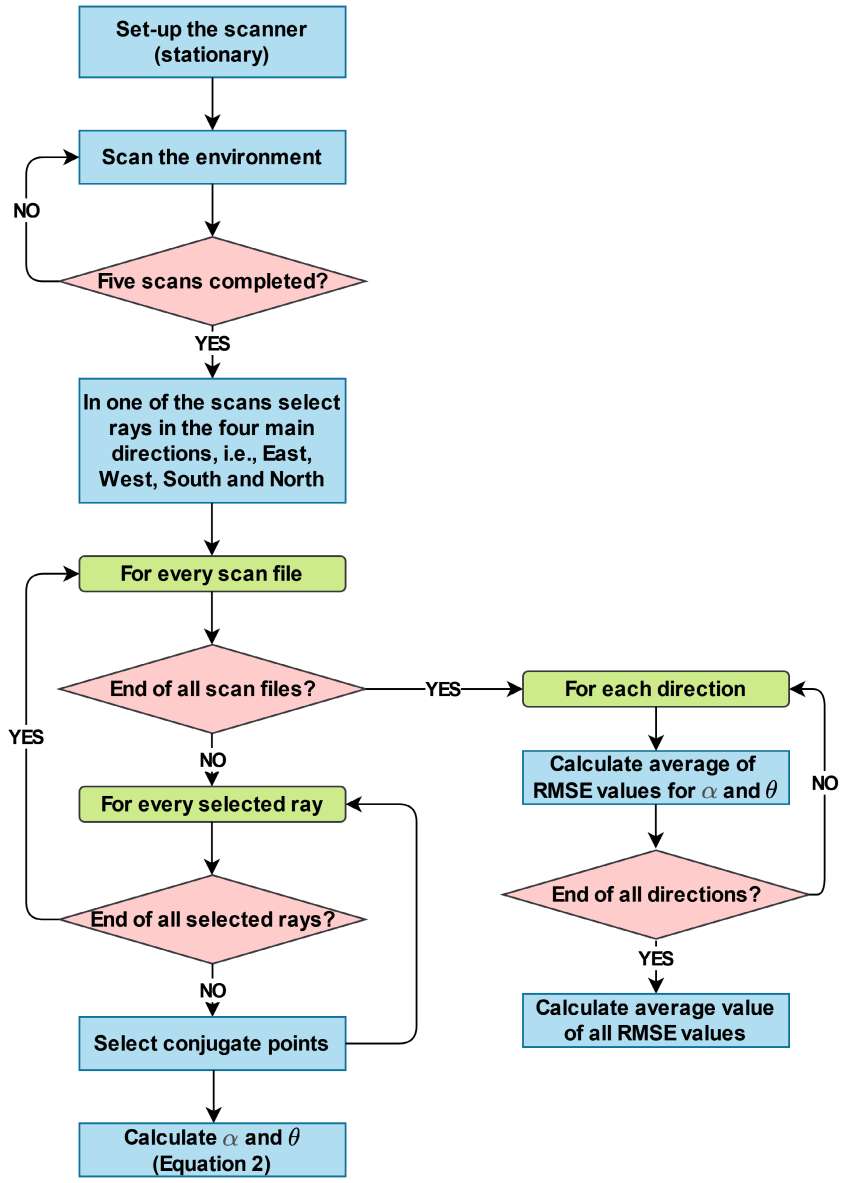


**FIGURE 2** Workflow of the angular precision ($\sigma_\alpha$, $\sigma_\theta$) determination.

computed by averaging the four RMSEs. For a detailed description of angular precision derivation, see Ozendi et al. (2016, 2017).

## Derivation of the range precision value ($\sigma_\rho$)

The range precision ($\sigma_\rho$) of TLSs depends on both the object–space and sensor–space parameters. The parameters that have the most significant effect on range precision ($\sigma_\rho$) are the TLS-to-object distance, the reflectivity properties of the target object and the incidence angle of the incoming laser beam. Therefore, the range precision varies for every point of a scan file; it is a point invariant value.

Previously we comprehensively investigated the effects of these parameters and explicitly formulated the range precision $(\sigma_\rho)$ as a function of these parameters (Ozendi et al., 2016, 2017).

The range precision $(\sigma_\rho)$ of a TLS can be formulated as shown in Equation (9):

$$\sigma_\rho = \frac{c + d\rho + f(I)}{\cos(\gamma)} \tag{9}$$

and

$$f(I) = \begin{cases} a + b\rho^2, \text{for } I < I_T^b \\ 0, \text{elsewhere} \end{cases} \tag{10}$$

where $a, b, c$ and $d$ are the scanner (sensor space) parameters, which are constant for each scanner. Although the same scanner is used, computation of these parameters should be repeated in each scanning project. Symbol $\rho$ is the distance between TLS and object, $\gamma$ is incidence angle of the incoming laser beam which can be defined as the angle between the local surface normal and the laser beam. The symbol $I$ is the intensity value of the point. While coefficients $a, b, c$ and $d$ are constant for each scanner, observations $\rho, \gamma$ and $I$ are variable for each point.

Part $c + d\rho$ in Equation (9) is the linear distance error, where $c$ is the constant error and $d\rho$ is the proportional error, whose contribution increases linearly as the distance $\rho$ increases. The coefficient $d$ is a fractional number.

Function $f(I)$ in Equation (9) represents the error contribution due to the surface reflectivity of the target object. It is a quadratic function of the distance $\rho$ as given in Equation (10). Cubic functions can also be considered. It is a piecewise function so that only the black (or absorbing) objects whose intensities $I$ are less than the threshold $I_T^b$ can contribute to the error. Surfaces with lower reflectivity return less of the incoming laser signal, thus smaller intensities.

The linear distance error $c + d\rho$ and the target reflectivity error $f(I)$ are the additive terms in Equation (9). Denominator term $\cos(\gamma)$ is the error due to the signal incidence angle, which intensifies or attenuates magnitude of the additive error terms. The incidence angle $\gamma$ affects the strength of the returned signal. As the incoming signal diverges from the surface normal, that is, the incidence angle increases, the returned signal gets weaker, that is, it results in the deterioration of $\sigma_\rho$. The measure of this deterioration was already formulated as the cosine of the incidence angle ($\cos(\gamma)$) (Baselgia et al., 2014; Grant et al., 2012b; Hebert & Krotkov, 1992; Soudarissanane et al., 2011). On the other hand, the appropriate composition of the distance, reflectivity and incidence angle error terms in Equations (9) and (10) is the new approach in this proposed work.

Variables $\rho, \gamma$ and $I$ are the observations, therefore they can be derived from the scan data either directly or computationally.

Coefficients $a, b, c$ and $d$ are the scanner-specific parameters, which can be derived using a single scanning configuration. First, two highly absorbent planar objects (black plates) and two perfectly reflective planar objects (white plates) were prepared. One pair of plates (one black, one white) was placed at close range, and the other pair was placed at long range, such as at 10 and 90 m, respectively. Alternative distances were tested in the previous studies of Ozendi et al. (2016, 2017). They were oriented perpendicularly to the TLS so that the incidence angles became near-0°. Then, a single scan was performed. This workflow is shown in Figure 3.

Since the plates are planar objects, the least squares plane fitting was computed for each plate. Then, the RMSE of the off-plane distance $d_i$ was computed and represented by the symbol $m$.

$$m = \pm\sqrt{\frac{\sum d_i d_i}{n-1}}. \tag{11}$$

where $n$ is the number of points on the plate.

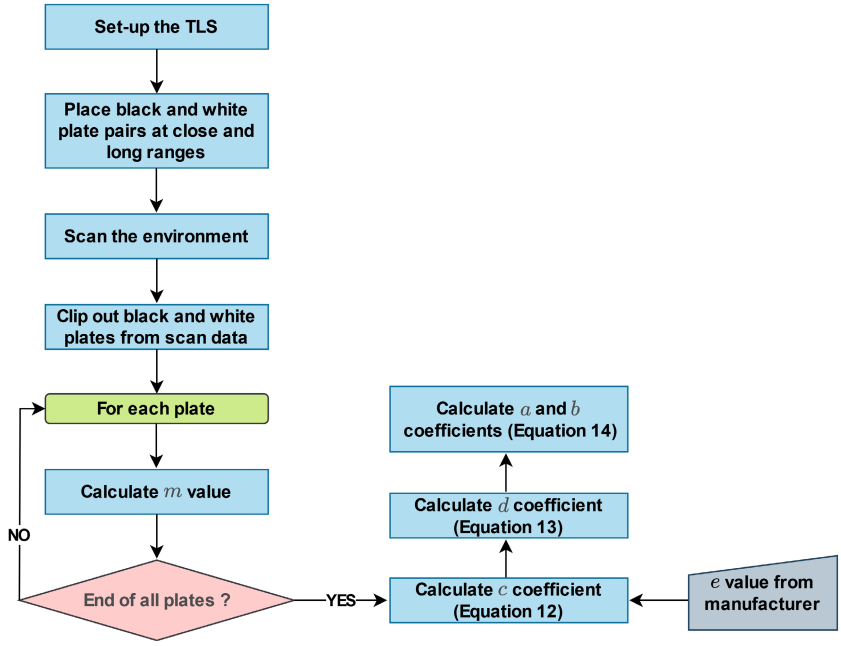


**FIGURE 3** Workflow of the range precision ($\sigma_\rho$) determination.

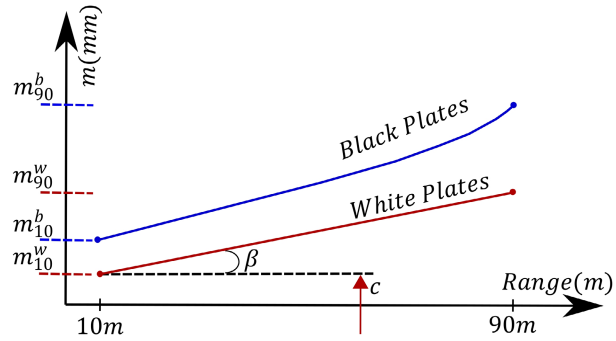


**FIGURE 4** Hypothetical graph of the four calculated *m* values.

The four $m^w_{10}$, $m^b_{10}$, $m^w_{90}$ and $m^b_{90}$ values are the RMS errors of the white plate at 10 m, the black plate at 10 m, the white plate at 90 m and the black plate at 90 m, respectively. Scanner-specific coefficients *a*, *b*, *c* and *d* can be calculated straightforwardly using the hypothetical graph in Figure 4.

The coefficient *c* is the summation of the constant distance accuracy (*e*), if provided by the manufacturer and $m^w_{10}$ which is the intercept of the red line (white plates) in Figure 4.

$$c = e + m^w_{10}. \tag{12}$$

The coefficient *d* is the slope of the red line (white plates) in Figure 4, which provides a linear interpolation of the errors due to the distance.

$$d = \frac{m^w_{90} - m^w_{10}}{90 - 10} = \tan(\beta). \tag{13}$$

Units of the numerator and denominator terms in Equation (13) should be equalised to metres or millimetres.

The reflectivity error $f(I)$ was computed only for the absorbent (black) objects. It is a kind of quadratic interpolation whose parameters $a$ and $b$ were calculated by solving the following equation system:

$$\begin{aligned} a + b\,10^2 &= m_{10}^b - m_{10}^w \\ a + b\,90^2 &= m_{90}^b - m_{90}^w. \end{aligned} \tag{14}$$

Units of the left- and right-side terms in Equation (14) should be equalised either to metres or millimetres.

Once the scanner invariant coefficients $a, b, c$ and $d$ were calculated, the range precision $\sigma_\rho$ of each point could be calculated using Equations (9) and (10).

Because all elements of matrix $\sum_{rr}$ were determined at this stage, error ellipsoid parameters of each individual point could be calculated by solving Equations (6)–(8). The error ellipsoids are specific for each point as illustrated in Figure 5.

## THE LEAST ERRORS SURFACE RECONSTRUCTION

The target object must be scanned from multiple viewpoints to ensure complete coverage. This data acquisition strategy naturally causes some overlap between the consecutive scans. Thus, the surface is sampled redundantly in the overlapping parts by points of varying quality. When these points (with high and low quality) are merged to generate a surface mesh, the resulting output's quality is unfavourably affected.

The proposed methodology aims to exclude the low-quality points in the processing workflow and reconstruct a surface mesh with a predefined and uniform level of spatial quality. This is achieved through successive decimation steps which are designed to keep the points with the high spatial quality and eliminate those with low spatial quality from the overlapping areas. Figure 6 outlines the complete surface mesh generation workflow: The left side, the "Anisotropic Point Error Model", was detailed in the previous section (The Anisotropic Point Error Model) and the right side of the workflow, the "Least Errors Surface Reconstruction", will be described here.

The left side of the workflow (Figure 6) starts with the scanning and co-registration steps. During the scanning campaign in the field, a series of five (stationary and repetitive) scans were carried out for the vertical and horizontal angle precision determination. In one of these scans, two pairs of white and black plates, for example, printed papers, were located at close and long ranges, respectively, in order to determine the range precision. These are the extra fieldwork efforts for the point error model computation. The scanner-specific parameters, that is, the vertical and horizontal angle precision $\sigma_\alpha$ and $\sigma_\theta$ values, and the coefficients $a, b, c$ and $d$, were computed. Every point in every scan file was then sought out, and its associated error ellipsoid was computed.

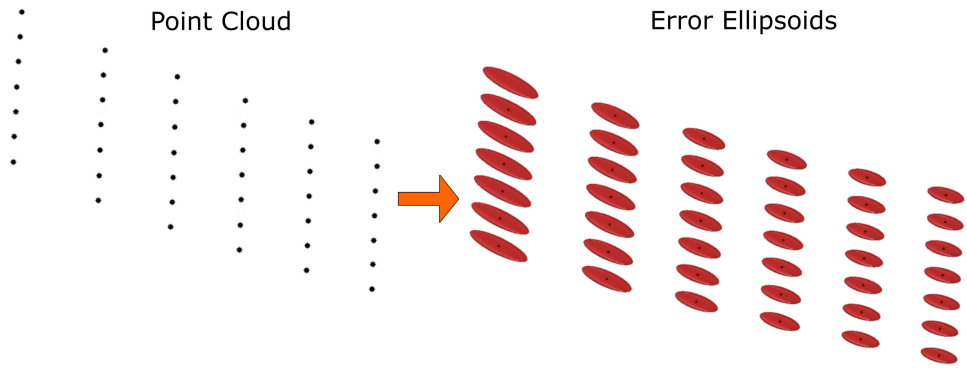


**FIGURE 5** Small set of points derived by TLS (left) and their corresponding error ellipsoids (right).

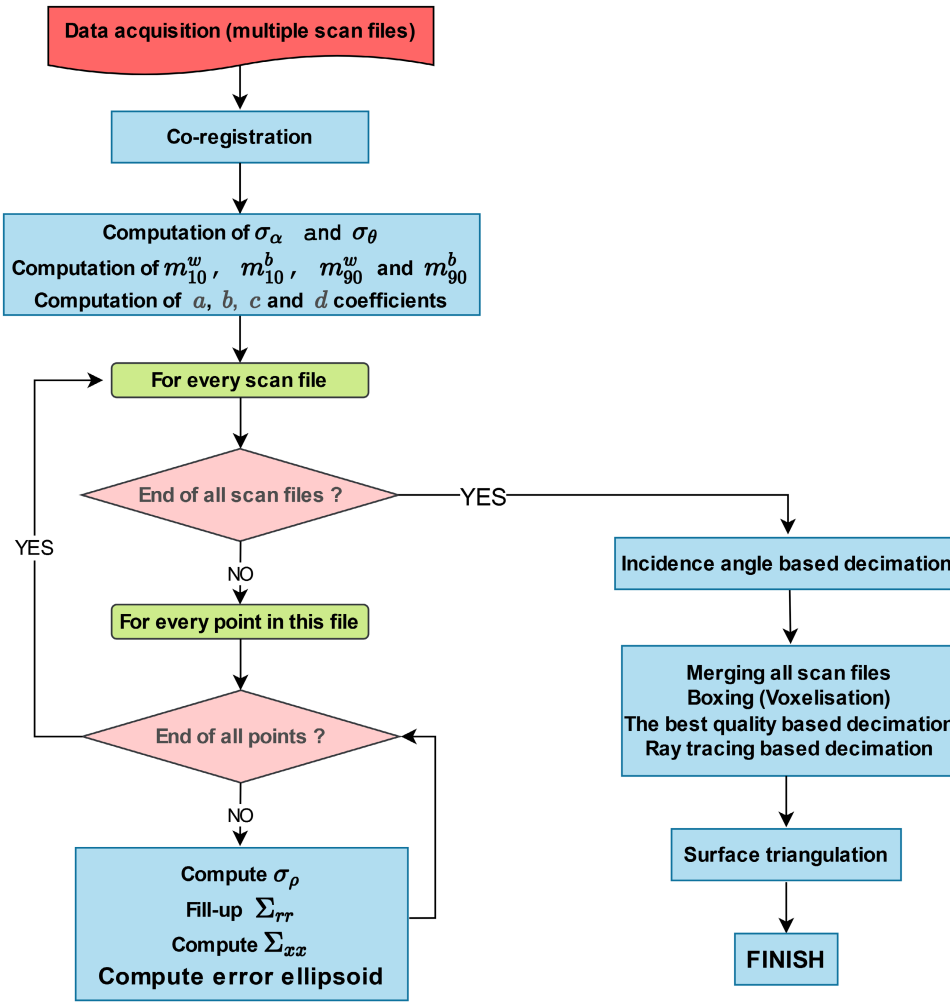


**FIGURE 6** Surface mesh generation workflow.

The right side of the workflow (Figure 6), the "Least Errors Surface Reconstruction" method, starts with the incidence angle-based decimation, in which points with large incidence angles are excluded. Then the complete set of scan files were merged and voxelised in a 3D boxing structure. The number of points may vary for each voxel, because the point density is not constant throughout the point cloud. The best quality point was selected in each voxel by evaluating its associated error ellipsoid. Thus, each voxel contains only 1 point. Ray tracing was then applied in order to exclude the obscured voxels which were stringed along the depth direction. Only the least erroneous points remained in the final step, which were the input to the subsequent surface triangulation step.

## Incidence angle-based decimation

The incidence angle-based decimation is the first step in eliminating low-quality points. High incidence angles cause weaker return signals from the object surface and consequently significant positional errors. Hence, the incidence angle ($\gamma$) strongly influences the geometric quality of the TLS points.

An incidence angle threshold ($t_\gamma$) was defined, and the points that exceeded this threshold were eliminated. The determination of the most appropriate $t_\gamma$ value is a heuristic process. There is always a trade-off between $t_\gamma$ and data completeness; for instance, selecting a smaller $t_\gamma$ will cause some data parts of the target object to be lost. In the experiments, $t_\gamma$ was usually selected as 60°.

Determination of the incidence angle threshold is difficult to automate as each scan dataset exhibits different characteristics. This issue is reflected in the experiments section where two different incidence angle thresholds are used in the monument dataset.

## Boxing (voxelisation)

The complete set of scan files was merged in the computer environment, and the scan file number of each point and the scan station information were saved.

Even though the points with high incidence angles were eliminated in the previous step, the overlapping areas in the point cloud still contained redundant data, including low- and high-quality points, that will cause errors, degradations and spurious triangulations in the resulting surface meshes. Therefore, the high spatial quality points should be kept, and the others should be eliminated. To achieve this, the merged point cloud was partitioned into small boxes or voxels. The box size should be carefully defined depending on the object to be modelled and the required level of detail so the target object's details are not lost.

Finally, the highest quality point for each box was determined using the associated error ellipsoid parameters. A positional quality is defined for each point using the error ellipsoid parameters. The definition of the quality metric and the way how it is used for filtering are described in the next step (see The Best Quality Point Based Decimation section) in detail.

The boxing structure used in this study is an extension of an algorithm for 3D point clouds (Akca & Gruen, 2005), initially developed by Chetverikov (1991) to perform neighbourhood search operations for planar point sets. This boxing algorithm was shown as an efficient method for creating organised or structured point cloud data from spatially non-ordered point lists (Akca, 2010). Moreover, it provides efficient access and query mechanisms. Implementation details are described by Akca (2010) and Akca and Gruen (2005).

## The best quality point based decimation

The set of points lying in each box was determined. The number of points may vary in each box, for example, null, 1 or more than 1 point, because the density is not constant throughout the point cloud. The error ellipsoid was used as a quality metric to select the best quality point in each box since its size, shape and orientation provide useful information about the positional quality of the point.

Each point is associated with its error ellipsoid whose semi-axis lengths are $\sqrt{\lambda_1}$, $\sqrt{\lambda_2}$ and $\sqrt{\lambda_3}$. Computational details are given in Anisotropic Point Error Model section. Here $\sqrt{\lambda_1}$ is the semi-major axis length along the ranging direction, and $\sqrt{\lambda_2}$ and $\sqrt{\lambda_3}$ are the semi-minor axes lengths along the lateral directions, which are perpendicular to the ranging direction (Figure 7). The semi-diagonal axis length of the bounding box of the error ellipsoid was selected as the quality metric $Q_i$ of any $i$-th point. It was computed as given in Equation (15):

$$Q = \sqrt{\left(\sqrt{\lambda_1}\right)^2 + \left(\sqrt{\lambda_2}\right)^2 + \left(\sqrt{\lambda_3}\right)^2}. \tag{15}$$

In this process step, the point with the minimum $Q_i$ value for each box was first selected, then the remaining points in this box were discarded. The resulting point cloud was thus composed of points whose error ellipsoids

have the minimum semi-diagonal axis length. Alternative approaches are also conceivable. All points in a box might be kept by weighting their contribution based on the $Q_i$ values.

At this step, each box contained only 1 point. Even though these points had the smallest $Q_i$ values, there may still have been some points with larger $Q_i$ values, especially where the surface had discontinuities. To eliminate these points, a heuristic threshold criteria $Q_T$ was defined, whose value was at the level of millimetres (e.g., 6 mm). Points that satisfied the condition $Q_i < Q_T$ were kept, and all the others were discarded. Care was also taken when selecting the $Q_T$ parameter; the smaller the $Q_T$, the higher the probability of loss in object details.

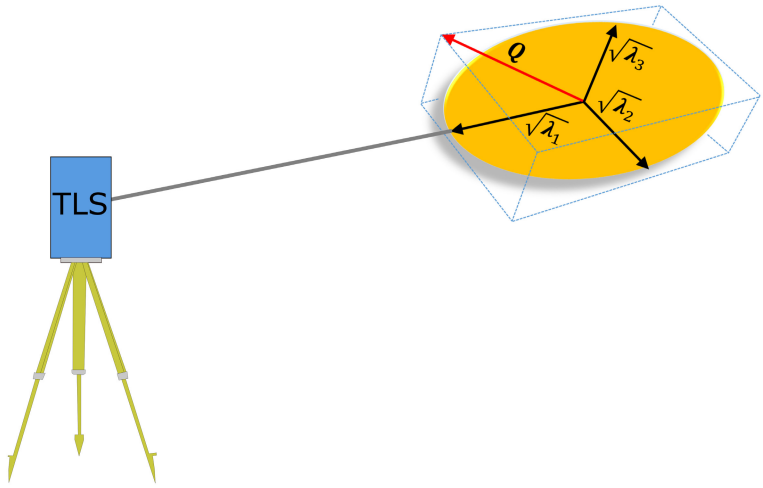


**FIGURE 7** Error ellipsoid of a point and its corresponding quality metric $Q_i$.

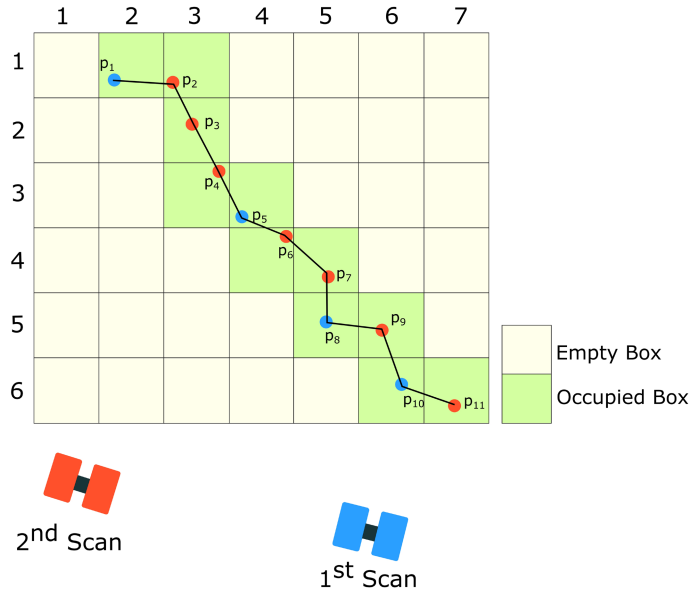


**FIGURE 8** Horizontal section of a boxing structure. The green boxes are occupied with points and the yellow boxes are empty. The blue points were acquired by the first scan and the red points were acquired by the second scan. The section of the mesh reconstructed from this point cloud is represented by the black polyline.

## Ray tracing based decimation (the Good, Bad, and the Better algorithm)

The best quality point-based decimation (in the previous step) effectively eliminates the low-quality points while keeping the highest quality point in each box. It sweeps the object's surface in the lateral direction. However, discretising the data space with boxes may result in redundant boxes along the depth direction, possibly obscuring each other so that the same surface part of the target object is sampled repetitively (Figure 8). Modelling problems arise if their spatial quality (i.e., quality metrics $Q_i$) have substantial differences.

Figure 8 illustrates that two scans sample the same portion of the target object. Since the incidence angles of the first scan are greater than the second scan, the $Q_i$ values of the first scan are greater than the $Q_i$ values of the second scan. Although points of the second scan (the red points) correctly depict the object surface, the contribution of the first scan (the blue points) disturbs the reconstructed mesh by producing spurious triangulations and artificial undulations like Moire stripes. Figure 9a,c shows a real example.

The Good, Bad, and the Better (GBB) algorithm was developed to solve this problem. This algorithm assigns a "GOOD", "BAD", and "BETTER" label to each point. First, all the points in the merged point cloud were visited. Then, a ray between the point and its scanner station was created for each point (Figure 10). Next, the ray was extended three box sizes so that the entire field of depth was travelled. Finally, all the boxes (and their points) intersected by the ray were listed using the Fast Voxel Traversal method (Amanatides & Woo, 1987).

The steps in the Good, Bad and The Better (GBB) algorithm are as follows:

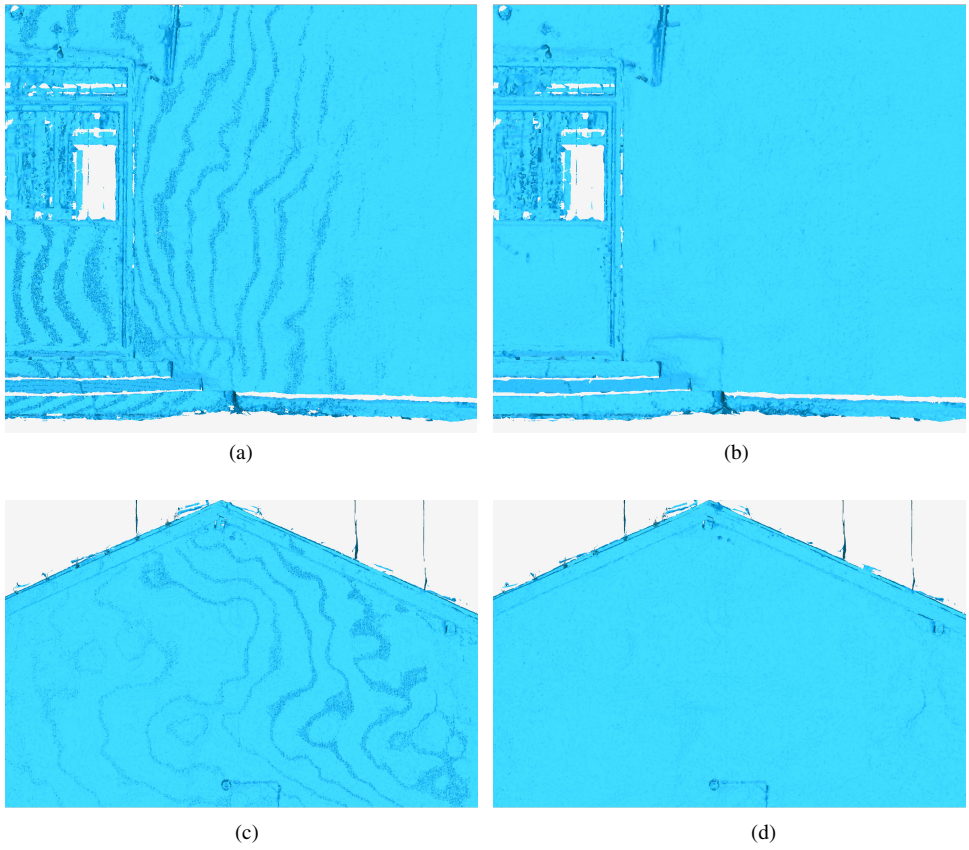


**FIGURE 9** (a–c) Result of the best quality point-based decimation step; and (b–d) result of the ray-tracing-based decimation step.

Step 1. Visit a point.

Step 2. Create its ray.

Step 3. List the intersected boxes. List their points. Ignore the empty boxes.

Step 4. Find the point with the smallest $Q_i$ value on this ray, and assign it a "GOOD" label; the remaining points of this ray will be assigned a "BAD" label.

- If the ray has only 1 point, it is automatically assigned a "GOOD" label.
- If a point has earned a "GOOD" label, it cannot be changed to a "BAD" label again.
- If the "GOOD" and/or "BAD" points from the previous rays are seen in this ray, include all of them and process them in the same way.
- If a "GOOD" point from the previous rays is seen in this ray, and if there exists another point with a smaller $Q_i$ value, keep the previously assigned "GOOD" label, and assign a "BETTER" label to this new point.

Step 5. Go to Step 1, if it is not at the end of the file.

Step 6. Finish.

The GBB algorithm is recursive: Any point is visited several times by several rays. The points assigned with the "BETTER" and "GOOD" labels will be used for the mesh reconstruction, while the points with the "BAD" label are discarded. Examples are shown in Figure 9b,d.

The GBB algorithm (Algorithm 1) can be implemented using the pseudo code shown below.

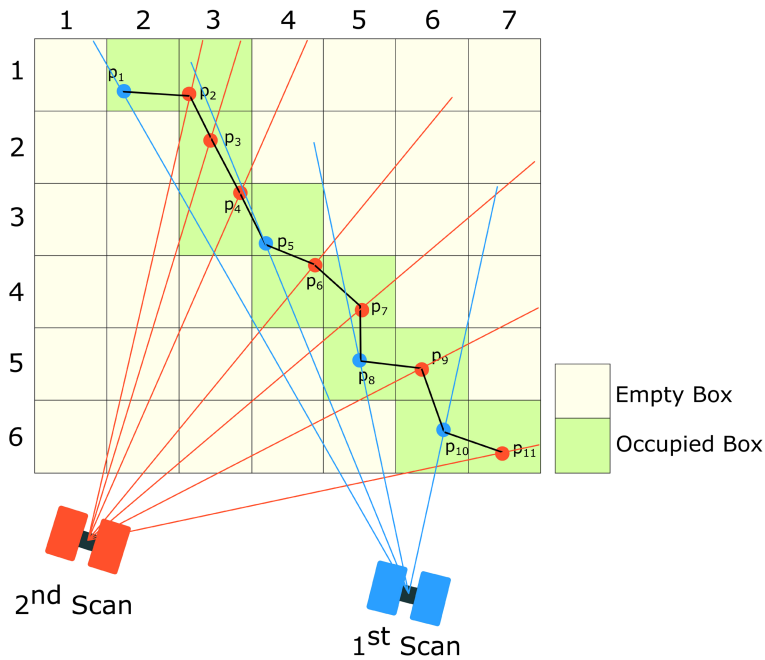


**FIGURE 10** Ray tracing of the points acquired from the two scan stations.

**Algorithm 1** **GBB Algorithm**

**Input:** Point cloud (number of points = n) with each point's ***Q*** value, Boxing Structure, TLS station coordinates, Label array ***L***.

**Output:** Set of Best Quality Points

1. Initialise ***L***, fill it with label {***BAD***}
2. For i = 1 to n
3. Calculate ray $\overrightarrow{\mathbf{R}_i}$ using $\overrightarrow{\mathbf{R}_i} = \boldsymbol{p}_i - \boldsymbol{p}_{i(TLS)}$ where, $\boldsymbol{p}_i = (x_i, y_i, z_i)$ and $\boldsymbol{p}_{i(TLS)} = (x_{i(TLS)}, y_{i(TLS)}, z_{i(TLS)})$
4. List Occupied Boxes (***OB***) that intersect the $\overrightarrow{\mathbf{R}_i}$
5. List ***Q*** values of points ***OB***(***Q***) corresponding to ***OB***
6. Point index with minimum ***Q*** value, ***indexMin*** = **min**(***OB***(***Q***))
7. Create a temporary array T1 which lists point indices corresponding to ***OB***
8. Crete a temporary array T2 which lists labels corresponding to T1
9. If all elements of T2 are BAD
10. Update ***L***, ***L***(***indexMin***) = ***GOOD***
11. Else
12. Create a temporary array T3 and assign point indices that have GOOD label in T2
13. Create a temporary variable T4 which stores the point index that has minimum ***Q*** value in T3
14. If ***Q*** **of** ***indexMin*** **is smaller than** ***Q*** **of** ***T4***
15. Update ***L***, ***L***(***indexMin***) = ***BETTER***
16. End If
17. End If
18. End For

Fill Best Quality Points array with the points with GOOD and BETTER labels

Return Best Quality Points

## Surface triangulation

The incidence angle-based decimation, the best quality point-based decimation, and the ray tracing-based decimation steps were applied. This step-by-step approach eliminates the low-quality points and keeps the points satisfying the predefined quality level. The remaining point cloud is now ready for input to the final surface triangulation step. Any academic or commercial software can be used for surface mesh generation.

# EXPERIMENTS AND RESULTS

## Data collection and pre-processing

The presented methodology was tested on two test objects: the Himmetoglu Primary School building and the Uzun Mehmet monument. The school building (Figure 11a) is located in Himmetoglu village (Zonguldak, Türkiye) and mainly contains planar surfaces. The monument, located in Zonguldak, a well-known coal-mining city (Figure 11b), was built in memory of mine martyrs, and unlike the school building, its structure is primarily curved.

All computations were programmed using the MATLAB environment; and Visualisation Tool Kit (VTK) and the Python programming language were used for visualisation purposes.


(a)

(b)

**FIGURE 11** Selected test objects: (a) The Himmetoglu Primary School building; and (b) The Uzun Mehmet monument.

The test objects were scanned using a Faro Focus 3D X330 TLS which was set to moderate resolution and quality parameters. A total of 23 scans of the school building, and eleven scans of the monument, were performed for complete coverage of both objects. To determine the error model parameters, five repetitive scans (each with the same scanning geometry and scanner station setup) were performed before both scanning campaigns.

As explained in the Anisotropic Point Error Model section, five repetitive scans acquired from the same station were needed to determine the angular precision. In addition, one scan was used to determine the range precisions in which two sets of black and white plate pairs were placed at close and long ranges. In the experiments, these plate pairs were placed at first, and then the scene was scanned five times. So that, the appropriate data set both

to determine the angular and range precisions was obtained. Two stands were used to hold the black and white plate pairs, which were backed by glass (alternative materials could also be used), in the experiments (Figure 12). A thin cardboard was painted with a black matte spray for the black plate and glued it onto the glass. A white cardboard was directly glued onto the glass for the white plate. Additionally, white strips were glued onto the edges of the black plate and black strips onto the edges of the white plate in order to make them clearly distinguishable in the point cloud (Figure 12).

**FIGURE 12** The stand holding the white (left) and black (right) plates.

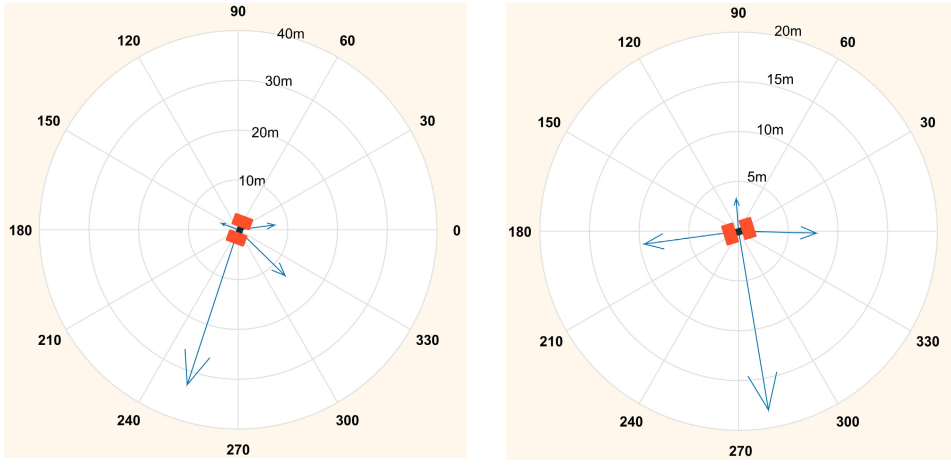


(a) (b)

**FIGURE 13** Top view of the selected four rays for the school building dataset (a) and the monument dataset (b). The rays are shown using blue arrows. The size of the arrow roughly shows the point to the TLS station distance. The TLS locations are represented using orange symbols.

**TABLE 1** Angular precisions in both datasets.

| Dataset | Vertical angle precision ($\sigma_\alpha$) | Horizontal angle precision ($\sigma_\theta$) |
|---|---|---|
| School building dataset | $20.1^{cc}$ | $85.9^{cc}$ |
| Monument dataset | $16.8^{cc}$ | $88.8^{cc}$ |

**TABLE 2** The $m$ values in both datasets.

| Dataset | Close range (m) | Long range (m) | $m^w_{Close}$ (mm) | $m^b_{Close}$ (mm) | $m^w_{Long}$ (mm) | $m^b_{Long}$ (mm) |
|---|---|---|---|---|---|---|
| School building dataset | 10 | 40 | 0.23 | 0.35 | 0.24 | 0.87 |
| Monument dataset | 10 | 90 | 0.22 | 0.39 | 0.54 | 2.30 |

**TABLE 3** Scanner invariant $a, b, c$ and $d$ parameters in both datasets.

| Dataset | $a$ | $b$ | $c$ | $d$ | $I^b_T$ [0–255] grey level |
|---|---|---|---|---|---|
| School building dataset | 8.619E−05 | 3.401E−07 | 2.23 | 3.833E−07 | 174 |
| Monument dataset | 1.469E−04 | 1.992E−07 | 2.22 | 3.929E−06 | 169 |

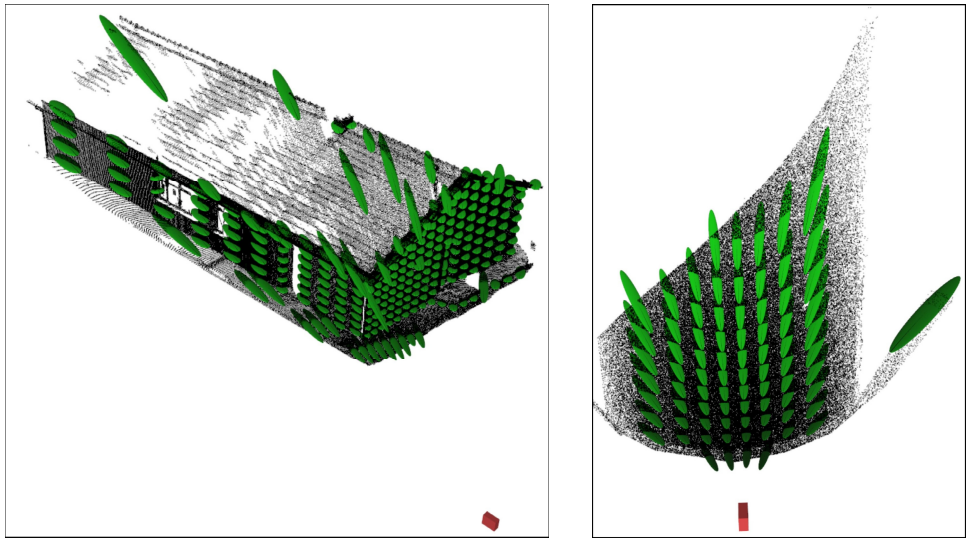

(a) (b)

**FIGURE 14** Sample point clouds and generated error ellipsoids of the school building (a) and the monument (b) datasets. The TLS stations are shown by the red cubes. For a better visualisation, the ellipsoids are plotted at every 50th point for the school building dataset and at every 200th point for the monument dataset.

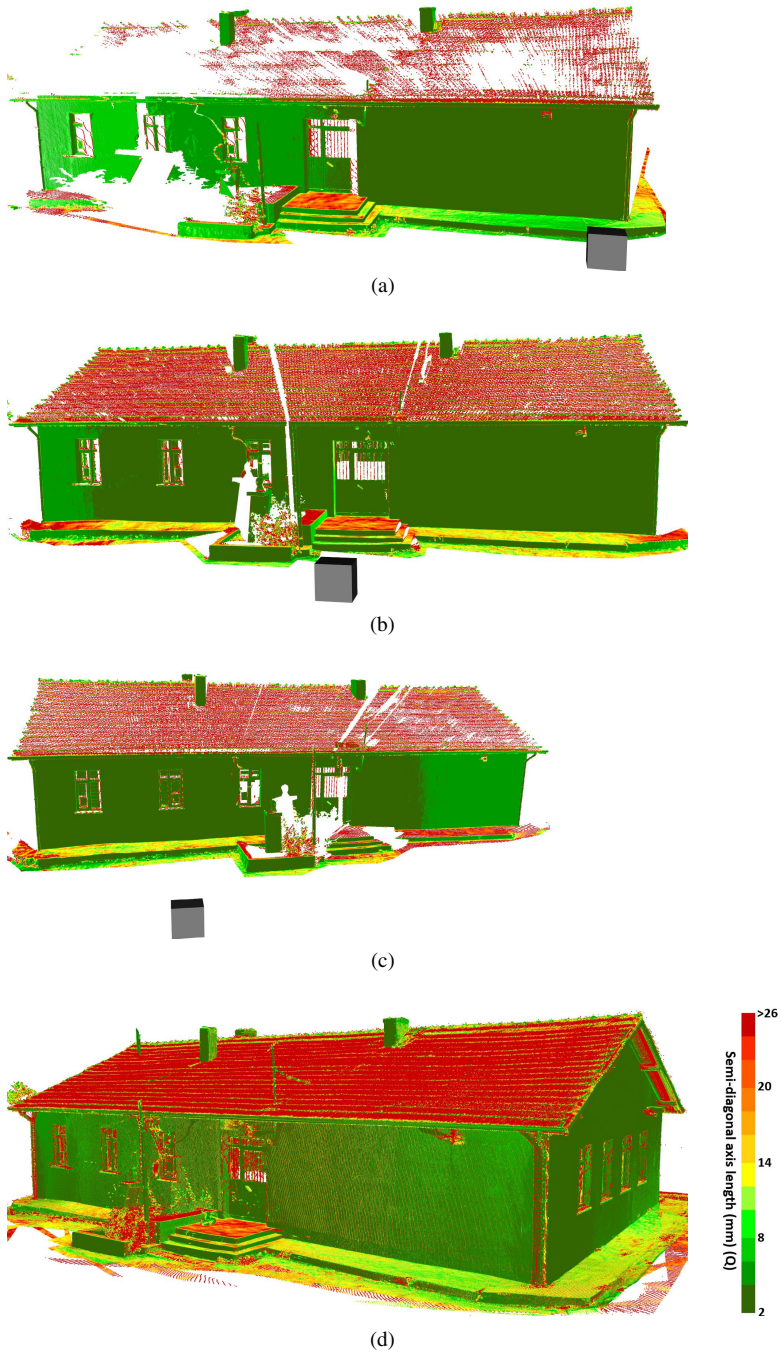


**FIGURE 15** Visualisation of the *Q* values. Three consecutive scans of the school building dataset in (a–c), and their merged file in (d). The points are coloured according to their *Q* values. The grey rectangular prisms in (a–c) show the scanner stations.

During the scanning campaign of the school building, the stands were placed 10 and 40 m away from the TLS. The stands were placed 10 and 90 m away for the monument. The stands were always placed perpendicular to the TLS position, so the incidence angles on the plates were close to zero.

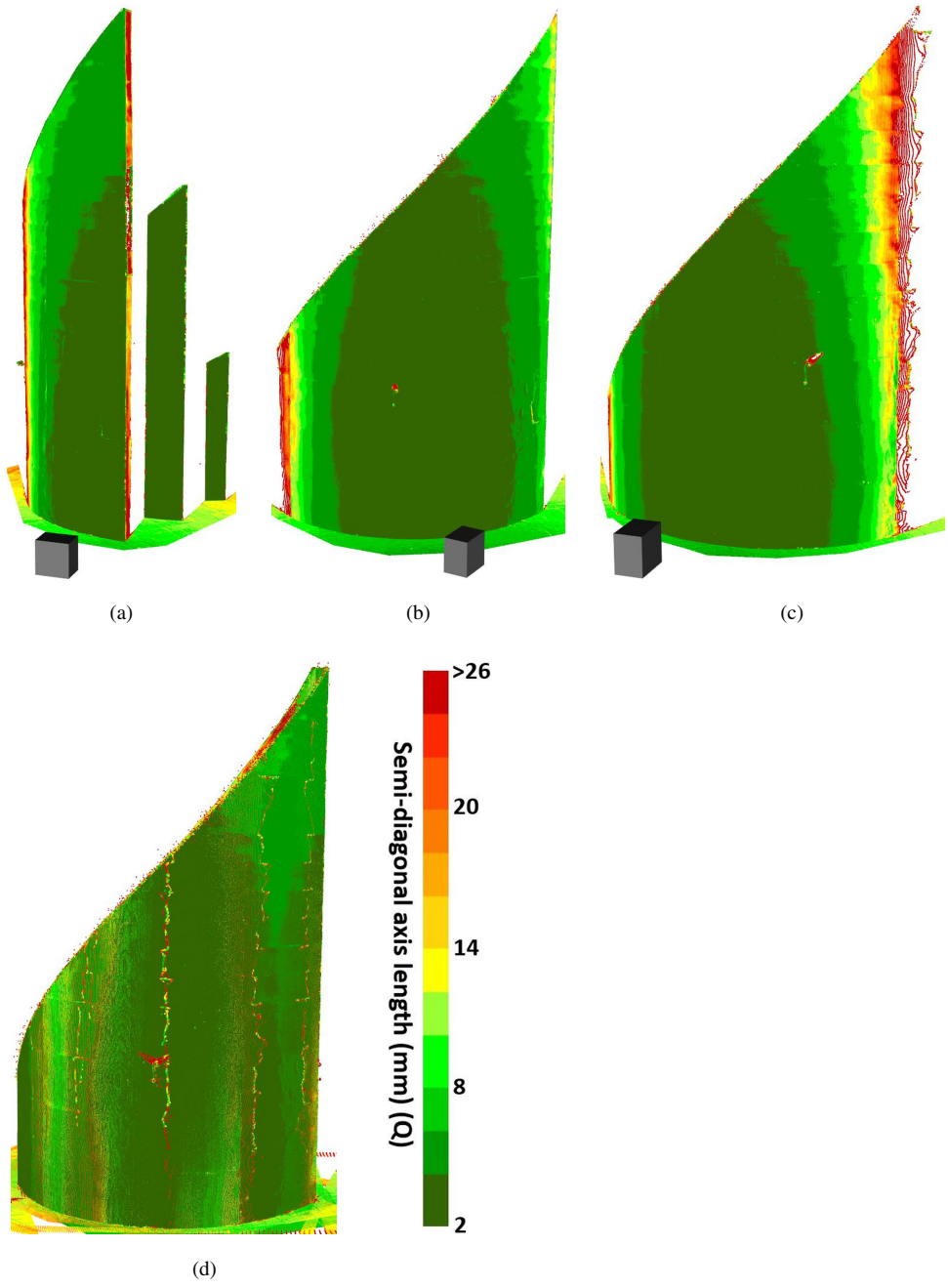


**FIGURE 16** Visualisation of the *Q* values. Three consecutive scans of the monument dataset in (a–c), and their merged file in (d). The points are coloured according to their *Q* values.

Both datasets were co-registered using Faro Scene v5.5, the Faro scanner's bundled software. The RMS errors of the co-registrations were reported as ±1.3 mm for the school building dataset and ±2.0 mm for the monument dataset. Following the co-registration process, error ellipsoids for each point of all the scans were computed.

## Error ellipsoid computation

### Vertical and horizontal angle precision $(\sigma_\alpha, \sigma_\theta)$ determination

The five repetitive scans were acquired from the same scanner station in both datasets. Four laser rays, each of which was approximately along the four cardinal directions, were selected. However, one ray in the school building dataset slightly deviated from its direction due to data availability problems (Figure 13a).

Then, conjugates of these rays in all five repeated scans were determined. Having obtained the five conjugate points for each direction, their corresponding vertical ($\alpha$) and horizontal ($\theta$) angles were calculated using Equation (2). In the next step, the root means square error (RMSE) values of both the vertical ($\alpha$) and horizontal ($\theta$) angles for each direction were computed. Finally, a priori angular precisions ( $\sigma_\alpha, \sigma_\theta$) were computed by averaging the four RMSEs. The results for each dataset are tabulated in Table 1. The estimated precisions were consistent across both datasets.

### Range precision $(\sigma_\rho)$ determination

One of the repeated scans was used to calculate the range precision ($\sigma_\rho$) in both datasets. The points belonging to the white and black plates were cropped and saved as different point cloud files. Then, the least squares plane fitting was performed for each file. Once the plane coefficients were obtained, the $m$ values of each plate for each dataset were calculated using Equation (11). These values are listed in Table 2.

Once the $m$ values in Table 2 were obtained, the scanner invariant $a, b, c$ and $d$ parameters were calculated in both datasets (Table 3) as described in the Derivation of the Range Precision Value section. The constant distance accuracy ($e$) was defined as 2 mm. The $I_T^b$ threshold value was calculated by averaging intensities of the black plates located at close and long ranges. The maximum of the average values was selected as $I_T^b$ in both datasets. All these scanner invariant parameters are shown in Table 3. Although two floating-point digits were used for the $m$ values in Table 2, their full digits were used to compute the parameters in Table 3.

Once the angular $(\sigma_\alpha, \sigma_\theta)$ and range precision $(\sigma_\rho)$ values were obtained, error ellipsoid parameters of any point could be computed as given in the Anisotropic Point Error Model section. The computed error ellipsoids are illustrated in Figure 14.

The ellipsoids become more elongated as the point to TLS station distances increase. Moreover, elongation of the ellipsoids becomes more drastic as the incidence angles increase. This relation is especially pronounced for the points on the ground and roof, where the incidence angles have larger values. Figure 14 shows that each point

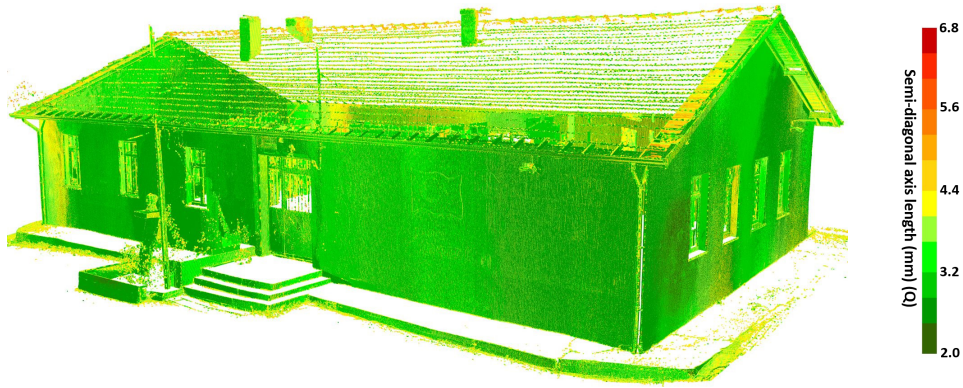


**FIGURE 17** Visualisation of the $Q$ values of the school building point cloud after the incidence angle-based decimation step with $t_\gamma = 60^o$.

in a point cloud has distinctive positional uncertainty. This information should be practically used when the noisy point cloud data is processed for 3D modelling.

## Quality metric computation

Once error ellipsoid parameters were obtained, the quality metric (Q) of each point was computed using Equation (15). Once the Q values were computed, all scan files were merged into one point cloud. The computed Q

**TABLE 4** Number of the points after each processing step.

| Processing step | School building dataset | Monument dataset |
|---|---|---|
| Original point cloud | 49,964,302 | 23,072,901 |
| Incidence angle-based decimation | 33,607,599 | 18,576,767 |
| Best quality point-based decimation | 5,934,665 | 3,902,931 |
| $Q_T$ threshold | 4,528,840 | 3,895,052 |
| Good, Bad, and the Better algorithm | 3,518,676 | 2,399,846 |

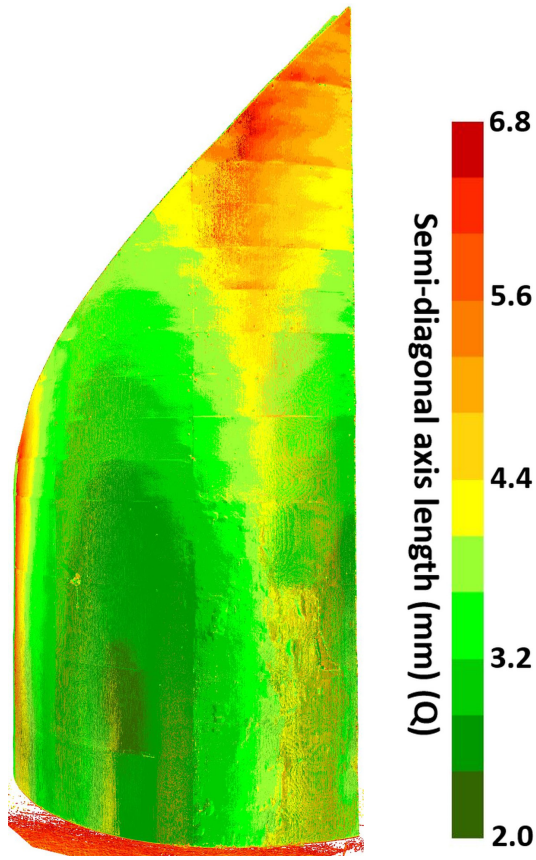


**FIGURE 18** Visualisation of the Q values of the monument point cloud after the incidence angle-based decimation step with $t_\gamma = 60^o$ and $t_\gamma = 70^o$.

values for some of the single scan files and their merged files are visualised in Figures 15 and 16 for the school building and the monument datasets, respectively.

The $Q$ value is represented in a colour scale in Figures 15 and 16, where green colour corresponds to high-quality, and red corresponds to low-quality points. The magnitude of the $Q$ value varies depending on the distance, incidence angle, and surface reflectance of the associated point.

Although the homogeneous colours at the foreground of the object surfaces (Figures 15d and 16d) seem to be the result of the mutually exclusive (independent) scans, this is not the fact, as this is an illusion of the point cloud visualisation. In reality, the foreground scan occludes the background overlapping scan(s) after a successful co-registration step. Therefore, the object surface is sampled using a mixture of the heterogeneous points from multiple scans, including both high- and low-quality points, even at the micro-scale. The proposed methodology detects and discards the low-quality points in the following processing steps.

## Incidence angle-based decimation

The incidence angle has a significant contribution to the error budget. As long as object completeness is not lost, points with higher incidence angles than the threshold $(t_\gamma)$ are to be deleted. For the school building dataset, the threshold value $t_\gamma$ was selected as 60° (Figure 17). Even though most of the roof and ground points were

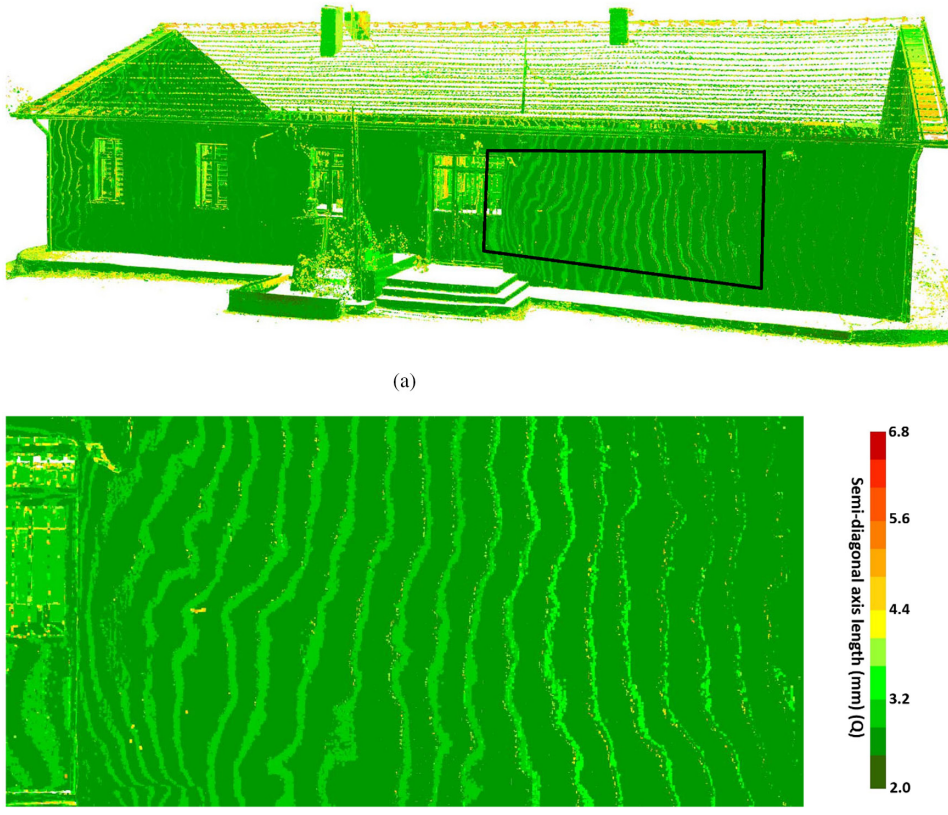


**FIGURE 19** Visualisation of the school building dataset after the boxing structure (a); close view of the region indicated by the black rectangle is shown in (b).

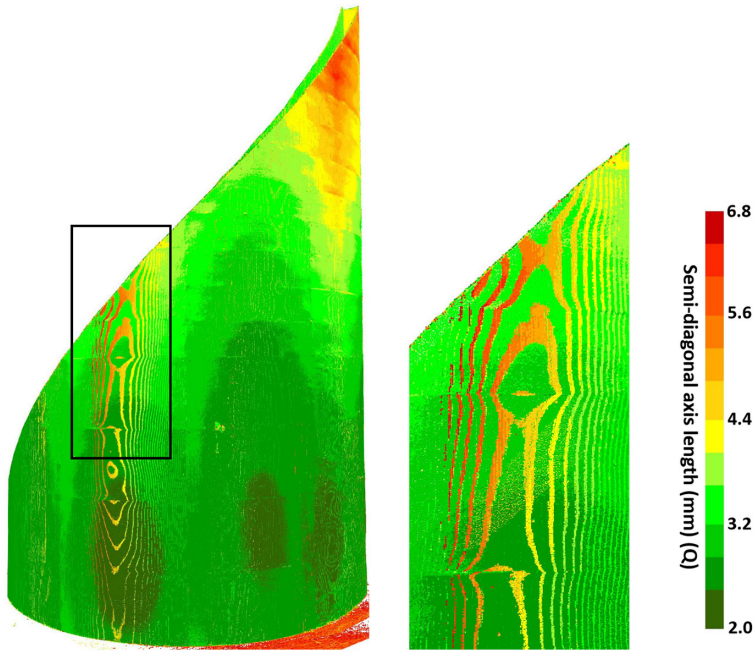


**FIGURE 20** Visualisation of the monument dataset after the boxing structure (a); close view of the region indicated by the black rectangle is shown in (b).

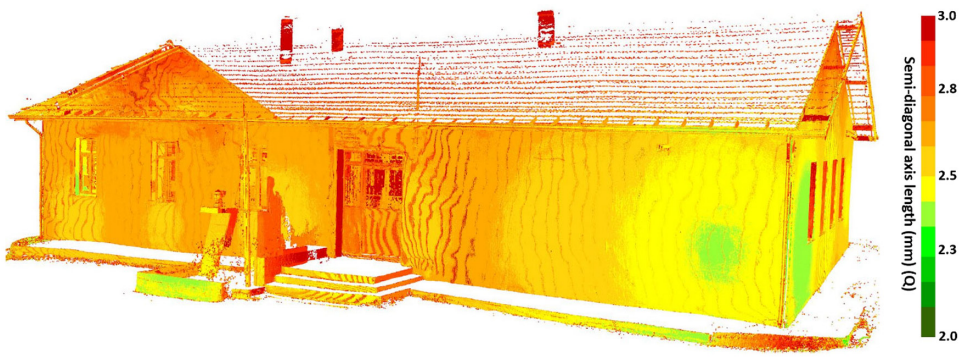


**FIGURE 21** Visualisation of the school dataset after the $Q_T$ threshold. Points satisfying the condition $Q > (Q_T = 3\,\text{mm})$ were discarded.

eliminated, the remaining points on the facades were enough to model the building. When compared to the original point cloud (Figure 15d), most of the low-quality points were eliminated (Table 4).

In the case of the monument dataset, selecting a single $t_\gamma$ value of 60° caused data loss at the upper parts of the object (Figure 18). However, it was understood that data loss occurs at the upper three scans when the $t_\gamma$ value is selected as 60°. Therefore, the $t_\gamma$ value was selected as 70° for only these three scans. For the remaining scans, the $t_\gamma$ value was selected as 60°. This dual thresholding approach solved the data loss problem by guaranteeing the object's completeness.

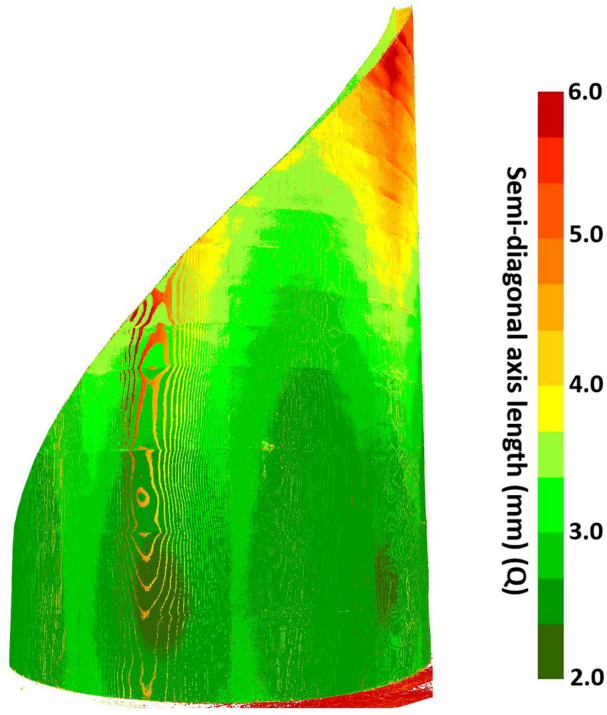


**FIGURE 22** Visualisation of the monument dataset after the $Q_T$ threshold. Points satisfying the condition $Q > (Q_T = 6\,\text{mm})$ were discarded.

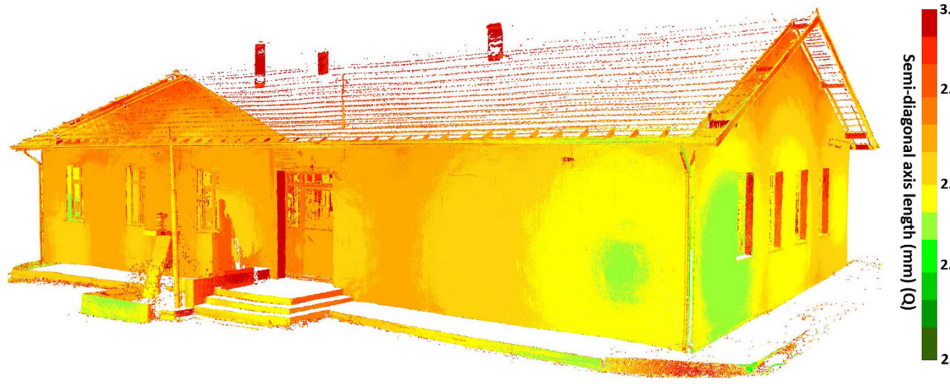


**FIGURE 23** Visualisation of the school building dataset after the GBB algorithm. Points with the "GOOD" and "BETTER" labels are shown.

## Best quality point-based decimation

The dataset was decimated using the boxing structure to reduce redundancy, which primarily existed in the overlapping parts of the scans. When selecting the box size, the detectable (small) feature size in the object–space and the point density in the data space should be collaterally considered. After several sizes were tested, an 8 mm box size was selected for both datasets in the experiments. The redundant points in the boxes were decimated so that

only the best quality point, based on its Q value, was retained in a box (Figures 19 and 20). The remaining points were discarded (Table 4).

Even though the number of points was significantly reduced by eliminating many low-quality points (Table 4), the object completeness was maintained in both datasets. However, erroneous points still exist as some of the best quality points of the boxes might have relatively larger error ellipsoids. Therefore, an upper bound must be defined by setting a user-defined threshold value $Q_T$. The threshold $Q_T = 3\ mm$ was selected for the school building dataset and $Q_T = 6.5\ mm$ for the monument dataset. The low-quality points with $Q > Q_T$ were discarded from both datasets (Figures 21 and 22).

## Ray tracing-based decimation (the Good, Bad, and the Better algorithm)

Since some occupied boxes obscured each other along the depth direction, artificial undulations like Moire stripes were still present in both datasets (Figures 21 and 22); the GBB algorithm was used to remove these stripe-formed artefacts (see the Ray Tracing Based Decimation in The Good, Bad, and the Better Algorithm section). The GBB algorithm preserved the points with "GOOD" and "BETTER" labels and discarded the "BAD" ones (Figures 23 and 24).

The GBB algorithm successfully removed the stripe-formed artefacts in the final processing step, as shown in Figures 23 and 24, with excellent performance.

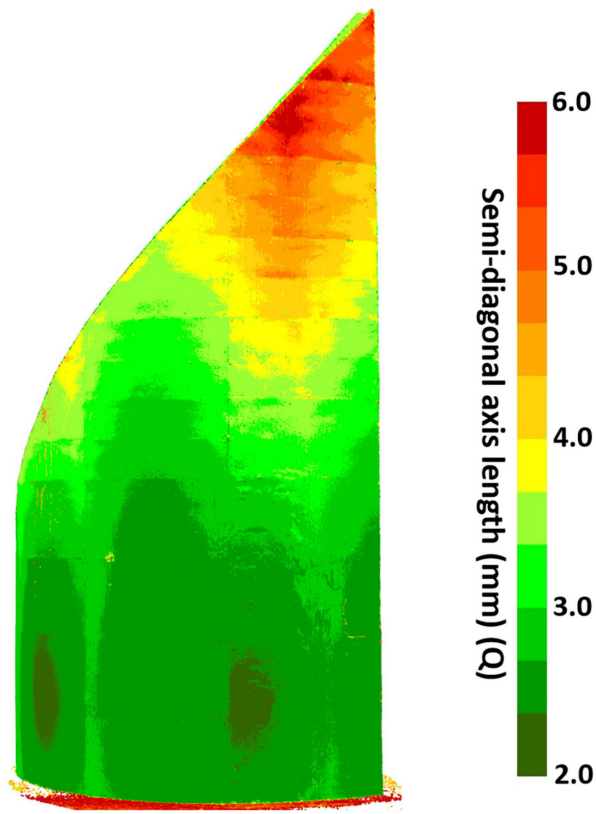


**FIGURE 24** Visualisation of the monument dataset after the GBB algorithm. Points with the "GOOD" and "BETTER" labels are shown.

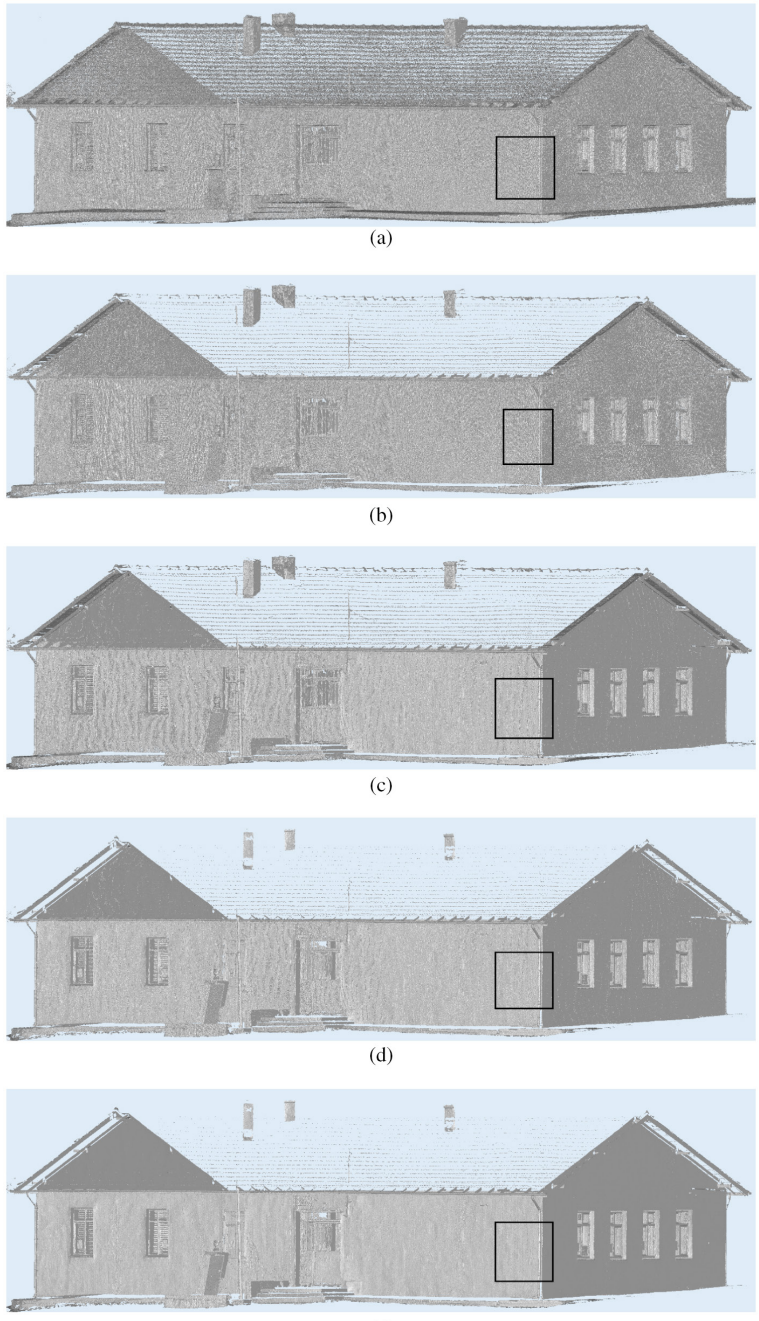


**FIGURE 25** 3D surface meshes of the school building dataset: (a) surface mesh generated from the original point cloud; (b) after the incidence angle-based decimation; (c) after the best quality point-based decimation; (d) after the $Q_T > 3$ mm threshold; (e) after the Good, Bad, and the Better algorithm; and (f–j) the zoom-in views of the areas marked with the black rectangles, respectively.

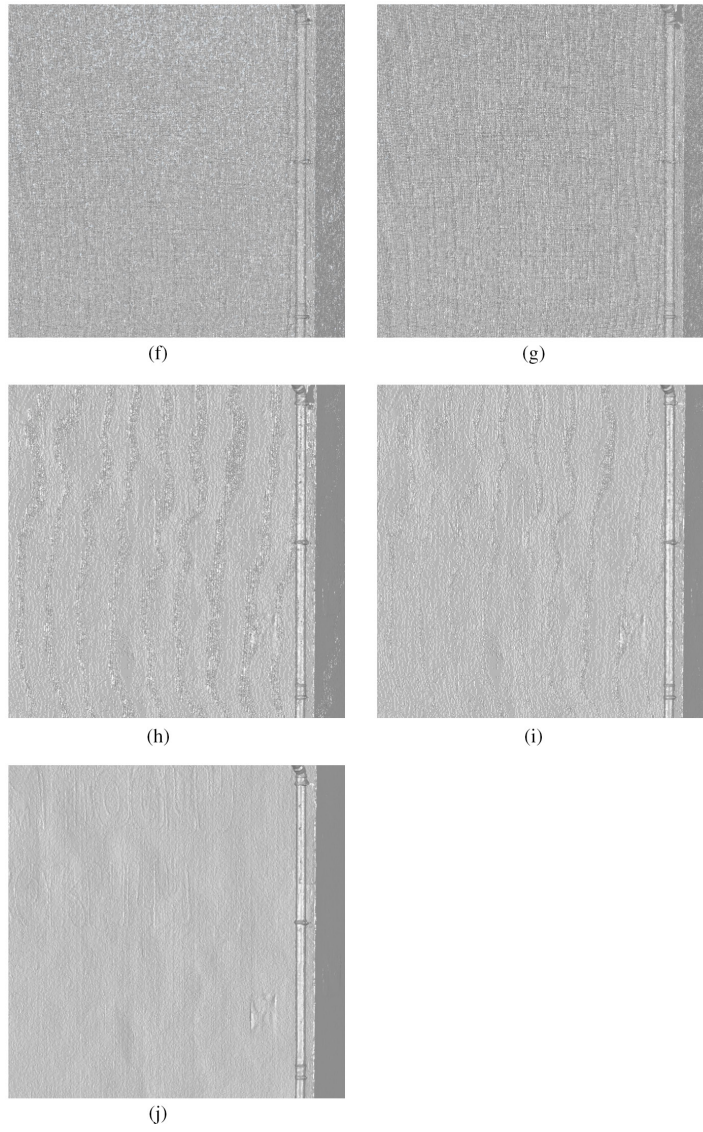


**FIGURE 25** (Continued)

In conclusion, the number of points was significantly reduced through these processing steps without scarifying the data completeness (Table 4). For example, the number of points in the school dataset was reduced by a factor of 14 and the monument dataset by a factor of 10. This reduced set of points facilitates the surface mesh generation process, with a spatial quality within a predefined interval.

## Surface mesh reconstruction

The final point cloud was optimised (in the previous steps) for 3D surface mesh generation as follows:

- Only points with the highest positional quality remained from the original noisy point cloud.

- It maintained coverage of entire target object and data loss within tolerable limits.
- The data volume was significantly reduced, which eases data management and surface mesh reconstruction tasks.

The Geomagic Wrap software (2021.2.1:64bit edition version) was used for 3D surface mesh generation. It is a commercial software that can import numerous data formats and export the surface mesh in many formats. Geomagic Wrap uses a Delaunay-based 3D triangulation algorithm developed by Edelsbrunner et al. (1998). A workstation with Intel® Core™ i9 2.40GHz CPU, 64 GB RAM, and NVIDIA Quadro RTX 4000 graphics card was used as the hardware.

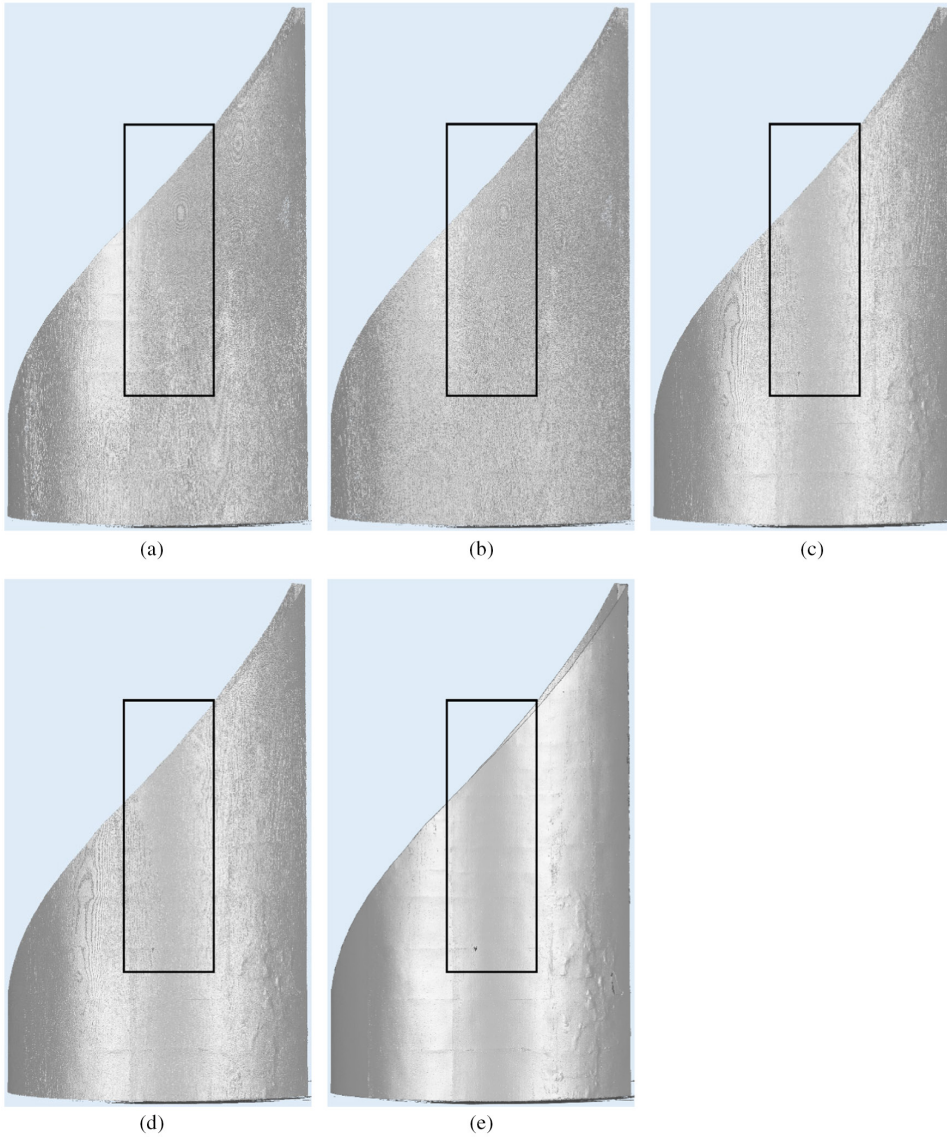


**FIGURE 26** 3D surface meshes of the monument dataset: (a) surface mesh generated from the original point cloud; (b) after the incidence angle-based decimation; (c) after the best quality point-based decimation; (d) after the $Q_T > 6.5$ mm threshold; (e) after the Good, Bad, and the Better algorithm; and (f–j) the zoom-in views of the areas marked with the black rectangles, respectively.

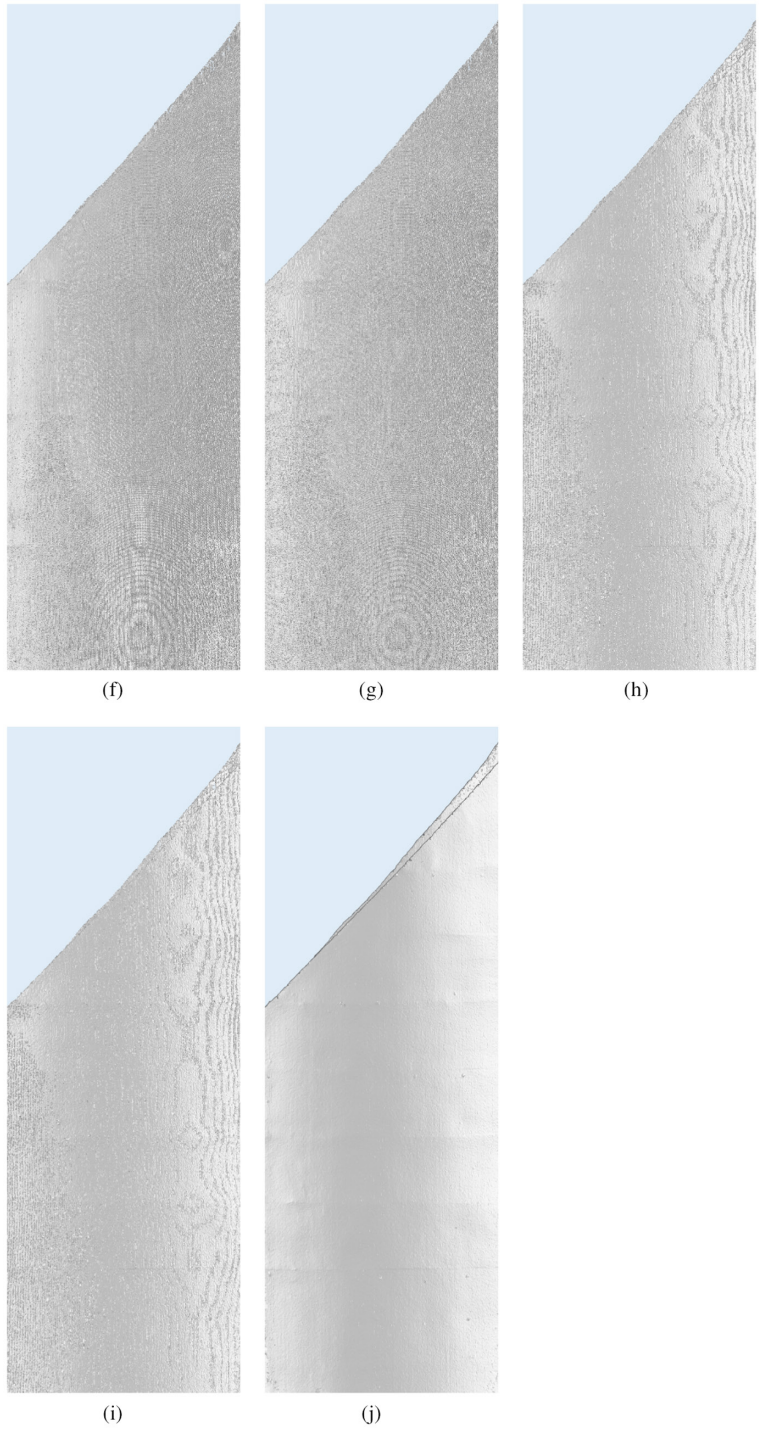


**FIGURE 26** (Continued)

Figures 25 and 26 illustrate the surface meshes generated from the school building and monument datasets. 3D surface mesh of the original point cloud was first generated from each dataset. Then, step-by-step, surface meshes from the successive decimation steps were generated to observe the mesh reconstruction performance

**TABLE 5** Triangle count and processing time of each surface mesh generation step.

| | School building dataset | | Monument dataset | |
|---|---|---|---|---|
| **Processing step** | **Triangle count** | **Time (s)** | **Triangle count** | **Time (s)** |
| Original point cloud | 80,335,160 | 567 | 41,759,228 | 255 |
| Incidence angle-based decimation | 60,294,987 | 378 | 34,238,074 | 209 |
| Best quality point-based decimation | 11,394,302 | 62 | 7,748,606 | 39 |
| $Q_T$ threshold | 8,829,291 | 45 | 7,733,973 | 38 |
| Good, Bad, and the Better algorithm | 6,897,478 | 34 | 4,781,847 | 21 |

of each processing step. The figures show the gradual improvement of the 3D surface meshes' quality through each processing step.

The final outputs displayed in Figures 25e and 26e were reached through a fully automated process and achieved successful results. The enlarged views in Figures 25j and 26j show the exceptional quality of the reconstructed surface meshes. Interestingly, part of the text "HİMMETOĞLU İLKOKULU" from the school building's façade (Figure 11a) is visible in the 3D model (upper part of Figure 25j). This phenomenon is result of range artefacts due to the intensity discontinuity in the object's surface. It has already been reported with the high accuracy (100 μm or better) point clouds acquired by the very short-range structured light and laser scanning systems in the past (Akca, 2007; Blais et al., 2005). However, this is the first time it has been observed in mm-level accuracy point clouds acquired by the middle-range TLS systems. This peculiar example proves the exceptional capability of the proposed methodology to model the object's surface accurately.

Table 5 displays the number of triangles generated in each step together with the processing times. The proposed methodology eliminates not only the erroneous but also the redundant points. Accordingly, the number of required triangles was reduced by a factor of 12 in the school building dataset and a factor of 9 in the monument dataset. Similarly, processing time was reduced by a factor of 17 in the school building dataset and a factor of 12 in the monument dataset.

The proposed stochastic surface mesh reconstruction approach results in accurate surface models with fewer triangle counts and reduced 3D triangulation time. It is an achievement to represent and model real-world objects within predefined tolerance limits.

## CONCLUSIONS

Over the past decade, the need for high-quality geospatial data has driven the development of TLS technology and its applications in many fields. TLSs capture object geometry in the form of dense, high-accuracy point clouds, which are used for 3D mesh generations of objects. However, point cloud data are subject to numerous errors that propagate into applications in the 3D mesh generation process. The ability to efficiently and accurately estimate these point errors and to identify and discard erroneous points is a critical research area with remaining shortfalls. This research offers a solution to these deficiencies through a novel two-part methodology for determining the highest quality data points to be used in surface mesh generation:

First, a novel anisotropic point error model was developed in which angular and range precisions were determined using a practical fieldwork. Unlike other methods that focus on single error sources, the proposed method

quantifies several dominant error sources (mechanical stability, distance, surface reflectivity, and incidence angle) into a total error budget for each point in the form of an error ellipsoid.

Second, a novel point cloud processing chain was developed resulting in high-quality surface mesh generations. This method removed low-quality points through successive decimation steps (incidence angle, best-quality point, ray tracing based) and proved highly successful; it retained only the points satisfying the user-defined positional quality level in the final point cloud.

The ray tracing-based decimation, namely the GBB algorithm, developed in this study is also novel; it effectively eliminated the stripe-like errors, which typically exist in the depth direction of the overlapping scans.

Additionally, two case studies, a planar school building and a curved monument, were used to test the newly developed methods, both of which resulted in high-quality surface mesh models.

The advantageous aspects of this methodology can be summarised as follows:

- It can be applied to all TLS brands.
- It quantises the positional quality of each point individually.
- It can automatically select the points with high positional quality.
- The proposed procedure efficiently models the random error pattern of each point in an anisotropic way.
- The redundant data is eliminated without any manual editing.
- It requires no post-processing of the output, such as mesh smoothing.
- It does not sacrifice data quality.
- It is easy to implement, practical, efficient and generic.

In the TLS used modelling projects, the workload for editing the acquired point clouds is much greater than the scanning campaign itself. The developed methodology is fully automated and shortens this time substantially. This research not only offers practical and efficient implementation at an academic level but also makes an effort to solve an industry problem. It is a complete solution covering the entire workflow from data acquisition in the fieldwork through 3D mesh model generation in the office. The proposed methodology results in high-quality surface mesh models with less office labour. Therefore, it is an economic and of high quality solution to an industry challenge.

Moreover, presented methodology is flexible; further extensions allow fusion of point clouds from different TLS brands and combined modelling of multi-sensor point clouds from terrestrial and airborne platforms. Vendor-provided technical specifications of TLS are not required, and the basic parameters can easily be computed with a simple in-the-field setup, making it both generic and practical.

The proposed methodology can be used as part of the TLS projects in the industry with the advantages of both economy and quality.

## ACKNOWLEDGMENTS

This paper is an extended version of a study originally presented at the ISPRS TC II Mid-term Symposium “Towards Photogrammetry 2020”, held in Riva del Garda, Italy, 3–7 June 2018. We thank infoTRON (Istanbul) for providing the Geomagic Wrap software.

## FUNDING INFORMATION

This study was supported by TUBITAK – The Scientific and Technological Research Council of Türkiye (project ID: 115Y239); and the Scientific Research Projects of Zonguldak Bülent Ecevit University (project ID: 2015-47912266-01).

## ORCID

*Hüseyin Topan* https://orcid.org/0000-0001-8195-9333

## REFERENCES


Adamson, A. & Alexa, M. (2006) Anisotropic point set surfaces. In: *Proceedings of the 4th International Conference on Computer Graphics, Virtual Reality, Visualisation and Interaction in Africa*, Cape Town, South Africa, January, pp. 7–13. Available from: https://doi.org/10.1145/1108590.1108592

Akca, D. (2007) *Least squares 3D surface matching*. Ph.D. thesis. ETH Zurich, Switzerland: Institute of Geodesy and Photogrammetry.

Akca, D. (2010) Co-registration of surfaces by 3D least squares matching. *Photogrammetric Engineering and Remote Sensing*, 76(3), 307–318. Available from: https://doi.org/10.14358/PERS.76.3.307

Akca, D. & Gruen, A. (2005) Fast correspondence search for 3d surface matching. *International Archives of Photogrammetry, Remote Sensing and Spatial Information Sciences*, 36(Part 3/W19), 186–191.

Akca, D., Gruen, A., Alkis, Z., Demir, N., Breuckmann, B., Erduyan, I. & Nadir, E. (2006) 3D modeling of the Weary Herakles statue with a coded structured light system. *International Archives of Photogrammetry, Remote Sensing and Spatial Information Sciences*, 36(Part 5), 14–19.

Akca, D., Remondino, F., Novàk, D., Hanusch, T., Schrotter, G. & Gruen, A. (2007) Performance evaluation of a coded structured light system for cultural heritage applications. Videometrics IX, Proc. of SPIE-IS&T Electronic Imaging, San Jose (California), USA, January 29–30. *SPIE*, 6491, 64910V-1-12.

Amanatides, J. & Woo, A. (1987) A fast voxel traversal algorithm for ray tracing. *Eurographics*. Available from: https://doi.org/10.2312/egtp.19871000

Bae, K.-H., Belton, D. & Lichti, D.D. (2009) A closed-form expression of the positional uncertainty for 3D point clouds. *IEEE Transactions on Pattern Analysis and Machine Intelligence*, 31(4), 577–590. Available from: https://doi.org/10.1109/tpami.2008.116

Barbarella, M., Fiani, M. & Lugli, A. (2017) Uncertainty in terrestrial laser scanner surveys of landslides. *Remote Sensing*, 9(2), 113. Available from: https://doi.org/10.3390/rs9020113

Baselgia, C., Bosse, M., Zlot, R. & Holenstein, C. (2014) Solid model reconstruction of large-scale outdoor scenes from 3D Lidar data. In: Yoshida, K. & Tadokoro, S. (Eds.) *Field and service robotics: Results of the 8th international conference*. Berlin: Springer, pp. 541–554. Available from: https://doi.org/10.1007/978-3-642-40686-7_36

Blais, F., Taylor, J., Cournoyer, L., Picard, M., Borgeat, L., Dicaire, L.G., Rioux, M., Beraldin, J.-A., Godin, G., Lahanier, C. & Aitken, G. (2005) Ultra-high resolution imaging at 50 μm using a portable XYZ-RGB color laser scanner. In: *International Workshop on Recording, Modeling and Visualization of Cultural Heritage*, Ascona, May 22–27 (on CD-ROM).

Bolkas, D. & Martinez, A. (2018) Effect of target color and scanning geometry on terrestrial LiDAR point-cloud noise and plane fitting. *Journal of Applied Geodesy*, 12(1), 109–127. Available from: https://doi.org/10.1515/jag-2017-0034

Chen, X., Hua, X., Zhang, G., Wu, H., Xuan, W. & Li, M. (2015) Evaluating point cloud accuracy of static three-dimensional laser scanning based on point cloud error ellipsoid model. *Journal of Applied Remote Sensing*, 9(1), 095991. Available from: https://doi.org/10.1117/1.jrs.9.095991

Chen, X., Yu, K. & Wu, H. (2017) Determination of minimum detectable deformation of terrestrial laser scanning based on error entropy model. *IEEE Transactions on Geoscience and Remote Sensing*, 56(1), 105–116.

Chen, X., Zhang, G., Hua, X. & Xuan, W. (2016) An average error-ellipsoid model for evaluating TLS point-cloud accuracy. *The Photogrammetric Record*, 31(153), 71–87. Available from: https://doi.org/10.1111/phor.12136

Chetverikov, D. (1991) Fast neighborhood search in planar point sets. *Pattern Recognition Letters*, 12(7), 409–412. Available from: https://doi.org/10.1016/0167-8655(91)90298-z

Chow, J.C., Lichti, D.D. & Teskey, W.F. (2010) Self-calibration of the Trimble (Mensi) GS 200 terrestrial laser scanner. *Proceedings of the International Archives of Photogrammetry, Remote Sensing and Spatial Information Sciences*, 38, 161–166.

Edelsbrunner, H., Facello, M., Fu, P., Qian, J. & Nekhayev, D. (1998) Wrapping 3D scanning data. In: Photonics West'98 Electronic Imaging. Available from: https://doi.org/10.1117/12.302448

Ge, X. & Wunderlich, T. (2016) Surface-based matching of 3D point clouds with variable coordinates in source and target system. *ISPRS Journal of Photogrammetry and Remote Sensing*, 111, 1–12. Available from: https://doi.org/10.1016/j.isprsjprs.2015.11.001

Grant, D., Bethel, J. & Crawford, M. (2012a) Point-to-plane registration of terrestrial laser scans. *ISPRS Journal of Photogrammetry and Remote Sensing*, 72, 16–26. Available from: https://doi.org/10.1016/j.isprsjprs.2012.05.007

Grant, D., Bethel, J. & Crawford, M. (2012b) Rigorous point-to-plane registration of terrestrial laser scans. *International Archives of Photogrammetry, Remote Sensing and Spatial Information Sciences*, 39(Part B5), 181–186. Available from: https://doi.org/10.5194/isprsarchives-XXXIX-B5-181-2012

Guehring, J. (2001) Reliable 3D surface acquisition, registration and validation using statistical error models. In: *Proceedings Third International Conference on 3-D Digital Imaging and Modeling*, Quebec City, QC, pp. 224–231. Available from: https://doi.org/10.1109/im.2001.924440

Guennebaud, G. & Gross, M. (2007) Algebraic point set surfaces. *ACM Transactions on Graphics*, 26(3), 23–es. Available from: https://doi.org/10.1145/1276377.1276406

Hartzell, P.J., Gadomski, P.J., Glennie, C.L., Finnegan, D.C. & Deems, J.S. (2015) Rigorous error propagation for terrestrial laser scanning with application to snow volume uncertainty. *Journal of Glaciology*, 61(230), 1148–1158. Available from: https://doi.org/10.3189/2015JoG15J031

Hebert, M. & Krotkov, E. (1992) 3D measurements from imaging laser radars: how Good are they? *Image and Vision Computing*, 10(3), 170–178. Available from: https://doi.org/10.1016/0262-8856(92)90068-E

Hildebrandt, K. & Polthier, K. (2004) Anisotropic filtering of non-linear surface features. *Computer Graphics Forum*, 23(3), 391–400. Available from: https://doi.org/10.1111/j.1467-8659.2004.00770.x

Hodge, R.A. (2010) Using simulated terrestrial laser scanning to analyse errors in high-resolution scan data of irregular surfaces. *ISPRS Journal of Photogrammetry and Remote Sensing*, 65(2), 227–240. Available from: https://doi.org/10.1016/j.isprsjprs.2010.01.001

Ingensand, H. (2006) Metrological aspects in terrestrial laser-scanning technology. In: *Proceedings of the 3rd IAG/12th FIG Symposium*, Baden, May 22–24.

Jones, T., Durand, F. & Desbrun, M. (2003) Non-iterative, feature-preserving mesh smoothing. *ACM Transactions on Graphics*, 22(3), 943–949. Available from: https://doi.org/10.1145/882262.882367

Kermarrec, G., Alkhatib, H. & Neumann, I. (2018) On the sensitivity of the parameters of the intensity-based stochastic model for terrestrial laser scanner. Case Study: B-Spline Approximation. *Sensors*, 18(9), 2964. Available from: https://doi.org/10.3390/s18092964

Kermarrec, G., Schild, N. & Hartmann, J. (2021) Using least-squares residuals to assess the Stochasticity of measurements—example: terrestrial laser scanner and surface modeling. *Engineering Proceedings*, 5(1), 59.

Lichti, D.D. (2007) Error modelling, calibration and analysis of an AM–CW terrestrial laser scanner system. *ISPRS Journal of Photogrammetry and Remote Sensing*, 61(5), 307–324. Available from: https://doi.org/10.1016/j.isprsjprs.2006.10.004

Lichti, D.D. (2010) Terrestrial laser scanner self-calibration: correlation sources and their mitigation. *ISPRS Journal of Photogrammetry and Remote Sensing*, 65(1), 93–102. Available from: https://doi.org/10.1016/j.isprsjprs.2009.09.002

Liu, S., Chan, K. & Wang, C.C.L. (2012) Iterative consolidation of unorganized point clouds. *IEEE Computer Graphics and Applications*, 32(3), 70–83. Available from: https://doi.org/10.1109/MCG.2011.14

Long, N.Q., Buczek, M.M., Hien, L.P., Szlapińska, S.A., Nam, B.X., Nghia, N.V. & Cuong, C.X. (2018) Accuracy assessment of mine walls' surface models derived from terrestrial laser scanning. *International Journal of Coal Science & Technology*, 5(3), 328–338.

Marton, Z.C., Rusu, R.B. & Beetz, M. (2009) On fast surface reconstruction methods for large and noisy point clouds. In: *2009 IEEE International Conference on Robotics and Automation*. Available from: https://doi.org/10.1109/robot.2009.5152628

Mezian, C., Vallet, B., Soheilian, B. & Paparoditis, N. (2016) Uncertainty propagation for terrestrial Mobile laser scanner. *International Archives of Photogrammetry, Remote Sensing and Spatial Information Sciences*, 41(Part B3), 331–335. Available from: https://doi.org/10.5194/isprs-archives-XLI-B3-331-2016

Ohtake, Y., Belyaev, A. & Seidel, H.-P. (2005) An integrating approach to meshing scattered point data. In: *Proceedings of the 2005 ACM Symposium on Solid and physical modeling*, Cambridge, Massachusetts, June 2005, pp. 61–69. Available from: https://doi.org/10.1145/1060244.1060252

Okatani, I.S. & Deguchi, K. (2002) A method for fine registration of multiple view range images considering the measurement error properties. *Computer Vision and Image Understanding*, 87(1–3), 66–77. Available from: https://doi.org/10.1006/cviu.2002.0983

Ozendi, M., Akca, D. & Topan, H. (2016) An Empirical point error model for Tls derived point clouds. International archives of photogrammetry. *Remote Sensing and Spatial Information Sciences*, 41(Part B5), 557–563. Available from: https://doi.org/10.5194/isprs-archives-XLI-B5-557-2016

Ozendi, M., Akca, D. & Topan, H. (2017) A generic point error model for TLS-derived point clouds. In: *Proc. SPIE 10332, Videometrics, Range Imaging, and Applications XIV*, Munich, Germany, 26 June. Available from: https://doi.org/10.1117/12.2269373

Parian, J.A. & Gruen, A. (2005) Integrated laser scanner and intensity image calibration and accuracy assessment. *Proceedings of the ISPRS Workshop Laser Scanning 2005*, XXXVI, 18–23.

Pauly, M. (2003) *Point primitives for interactive modeling and processing of 3D-geometry*. Zurich: Federal Institute of Technology (ETH) of Zurich. Available from: https://doi.org/10.3929/ethz-a-004612876

Pu, S. (2008) Automatic building modeling from terrestrial laser scanning. In: van Oosterom, P., Zlatanova, S., Penninga, F. & Fendel, E.M. (Eds.) *Advances in 3D Geoinformation systems*. Berlin: Springer, pp. 147–160. Available from: https://doi.org/10.1007/978-3-540-72135-2_9

Sagawa, R., Oishi, T., Nakazawa, A., Kurazume, R. & Ikeuchi, K. (2002) Iterative refinement of range images with anisotropic error distribution. *International Conference on Intelligent Robots and Systems, IEEE/RSJ*, 71, 79–85. Available from: https://doi.org/10.1109/irds.2002.1041366

Sagawa, R., Osawa, N., Echigo, T. & Yagi, Y. (2005) Real time 3D environment modeling for a mobile robot by aligning range image sequences, *Proceedings of the British Machine Vision Conference 2005*, Oxford, UK, September 2005, pp. 330–339. Available from: https://doi.org/10.5244/C.19.13

Sagawa, R., Osawa, N. & Yagi, Y. (2006) A probabilistic method for aligning and merging range images with anisotropic error distribution. In: *Proceedings of the Third International Symposium on 3D Data Processing, Visualization, and Transmission (3DPVT'06)*, pp. 559–566. Available from: https://doi.org/10.1109/3dpvt.2006.17

Scaioni, M. (2012) On the estimation of rigid-body transformation for TLS registration. *International Archives of Photogrammetry, Remote Sensing and Spatial Information Sciences*, 39(Part B5), 601–606. Available from: https://doi.org/10.5194/isprsarchives-XXXIX-B5-601-2012

Schall, O., Belyaev, A. & Seidel, H.-P. (2005) Robust filtering of noisy scattered point data. *Proceedings Eurographics/IEEE VGTC Symposium Point-Based Graphics*, 71–144. Available from: https://doi.org/10.2312/SPBG/SPBG05/071-077

Schmitz, B., Holst, C., Medic, T., Lichti, D.D. & Kuhlmann, H. (2019) How to efficiently determine the range precision of 3D terrestrial laser scanners. *Sensors*, 19(6), 1466. Available from: https://doi.org/10.3390/s19061466

Schulz, T. (2008) *Calibration of a terrestrial laser scanner for engineering geodesy*. PhD thesis. Zurich: Institute of Geodesy and Photogrammetry of the ETH Zurich.

Sofia, G., Pirotti, F. & Tarolli, P. (2013) Variations in multiscale curvature distribution and signatures of LiDAR DTM errors. *Earth Surface Processes and Landforms*, 38(10), 1116–1134.

Soudarissanane, S., Lindenbergh, R., Menenti, M. & Teunissen, P. (2011) Scanning geometry: influencing factor on the quality of terrestrial laser scanning points. *ISPRS Journal of Photogrammetry and Remote Sensing*, 66(4), 389–399. Available from: https://doi.org/10.1016/j.isprsjprs.2011.01.005

Stenz, U., Hartmann, J., Paffenholz, J.-A. & Neumann, I. (2020) High-precision 3D object capturing with static and kinematic terrestrial laser scanning in industrial applications—approaches of quality assessment. *Remote Sensing*, 12(2), 290. Available from: https://doi.org/10.3390/rs12020290

Tan, K., Zhang, W., Shen, F. & Cheng, X. (2018) Investigation of TLS intensity data and distance measurement errors from target specular reflections. *Remote Sensing*, 10(7), 1077. Available from: https://doi.org/10.3390/rs10071077

Wang, J., Xu, K., Liu, L., Cao, J., Liu, S., Yu, Z. & Gu, X.D. (2013) Consolidation of low-quality point clouds from outdoor scenes. *Computer Graphics Forum*, 32(5), 207–216. Available from: https://doi.org/10.1111/cgf.12187

Wang, X., Liu, X. & Qin, H. (2013) Robust surface consolidation of scanned thick point clouds. In: *2013 International Conference on Computer-Aided Design and Computer Graphics*, 16–18 Nov, pp. 38–43. Available from: https://doi.org/10.1109/CADGraphics.2013.12

Weyrich, T., Pauly, M., Keiser, R., Heinzle, S., Scandella, S. & Gross, M. (2004) Post-processing of scanned 3D surface data. In: *SPBG'04 Symposium on Point-Based Graphics 2004*, pp. 85–94. Available from: https://doi.org/10.2312/SPBG/SPBG04/085-094

Williams, J.A., Bennamoun, M. & Latham, S. (1999) Multiple view 3D registration: a review and a new technique. *Conference Proceedings of IEEE International Conference on Systems, Man, and Cybernetics, IEEE SMC'99*, 493, 497–502. Available from: https://doi.org/10.1109/icsmc.1999.823255

Winiwarter, L., Anders, K. & Höfle, B. (2021) M3C2-EP: pushing the limits of 3D topographic point cloud change detection by error propagation. *ISPRS Journal of Photogrammetry and Remote Sensing*, 178, 240–258.

Wujanz, D., Burger, M., Mettenleiter, M. & Neitzel, F. (2017) An intensity-based stochastic model for terrestrial laser scanners. *ISPRS Journal of Photogrammetry and Remote Sensing*, 125, 146–155. Available from: https://doi.org/10.1016/j.isprsjprs.2016.12.006

Wujanz, D., Burger, M., Tschirschwitz, F., Nietzschmann, T., Neitzel, F. & Kersten, T.P. (2018) Determination of intensity-based stochastic models for terrestrial laser scanners utilising 3D-point clouds. *Sensors*, 18(7), 2187. Available from: https://doi.org/10.3390/s18072187

Xingchang, L. & Xianlin, L. (2006) Reconstruction of 3D model based on laser scanning. In: Abdul-Rahman, A., Zlatanova, S. & Coors, V. (Eds.) *Innovations in 3D geo information systems*. Berlin: Springer, pp. 317–332. Available from: https://doi.org/10.1007/978-3-540-36998-1_25

Young Min, K., Chan, D., Theobalt, C. & Thrun, S. (2008) Design and calibration of a multi-view TOF sensor fusion system. In: *2008 IEEE Computer Society Conference on Computer Vision and Pattern Recognition Workshops*, 23–28 June 2008, pp. 1–7. Available from: https://doi.org/10.1109/CVPRW.2008.4563160

**How to cite this article:** Ozendi, M., Akca, D. & Topan, H. (2023) A point cloud filtering method based on anisotropic error model. *The Photogrammetric Record*, 38, 460–497. Available from: https://doi.org/10.1111/phor.12460